HHS Public Access

Author manuscript

Neuron. Author manuscript; available in PMC 2019 December 05.

Published in final edited form as:

Neuron. 2018 December 05; 100(5): 1180–1193.e6. doi:10.1016/j.neuron.2018.09.049.

Chd2 is necessary for neural circuit development and long-term memory

Young J Kim[1,*], **Sattar Khoshkhoo**[1,2], **Jan C Frankowski**[1], **Bingyao Zhu**[1], **Saad Abbasi**[1], **Sunyoung Lee**[1,3], **Ye Emily Wu**[4], and **Robert F Hunt**[1,5,*,+]

[1]Department of Anatomy & Neurobiology, University of California, Irvine, CA, 92697, USA

[2]Department of Neurology, Brigham and Women's Hospital, Harvard University, Boston, MA 02115

[3]Department of of Integrative Biology and Physiology, University of California, Los Angeles, CA 90095

[4]Department of Biological Chemistry and Department of Neurobiology, David Geffen School of Medicine, University of California, Los Angeles, CA 90095, USA

[5]Twitter: @hunt_lab

Summary

Considerable evidence suggests loss of function mutations in the chromatin remodeler, *CHD2,* contribute to a broad spectrum of human neurodevelopmental disorders. However, it is unknown how *CHD2* mutations lead to impaired brain function. Here we report mice with heterozygous mutations in *Chd2* exhibit deficits in neuron proliferation and a shift in neuronal excitability that included divergent changes in excitatory and inhibitory synaptic function. Further *in vivo* experiments show $Chd2^{+/-}$ mice displayed aberrant cortical rhythmogenesis and severe deficits in long-term memory, consistent with phenotypes observed in humans. We identified broad, age-dependent transcriptional changes in $Chd2^{+/-}$ mice, including alterations in neurogenesis, synaptic transmission and disease-related genes. Deficits in interneuron density and memory caused by $Chd2^{+/-}$ were reproduced by *Chd2* mutation restricted to a subset of inhibitory neurons and

*Correspondence: yjkim13@uci.edu or robert.hunt@uci.edu.
+Lead contact: robert.hunt@uci.edu

Author Contributions

Y.J.K. contributed to the design, execution and analysis of experiments, and wrote the manuscript. S.K., S.A., J.C.F. B.Z. and S.L. contributed to the execution and analysis of experiments, and helped edit the manuscript. Y.E.W. contributed to analysis of RNA-seq experiments. R.F.H. contributed to the concept, design, execution and analysis of experiments, funding, and wrote the manuscript.

Declaration of Interests

The authors declare no competing interests.

Data and Software Availability

All RNA-seq data are available in Tables S1 and S2; raw counts from RNA-sequencing are available on the Gene Expression Omnibus (GEO) repository (GSE112196). Data that support the findings of this study are available from the corresponding authors upon reasonable request.

corrected by interneuron transplantation. Our results provide initial insight into how *Chd2* haploinsufficiency leads to aberrant cortical network function and impaired memory.

Introduction

Exome sequencing studies have now identified hundreds of gene mutations carrying an increased risk for neurodevelopmental disorders (Epi4K Consortium et al., 2013; De Rubeis et al., 2014; Iossifov et al., 2014; Deciphering Developmental Disorders Study, 2015). Of these, mutations in genes encoding chromatin regulators have emerged as a common risk factor, with *CHD2*, a member of the chromodomain helicase DNA-binding (CHD) family of proteins, being frequently affected (Carvill et al., 2013; Carvill et al., 2015). *CHD2* is an ATP-dependent chromatin-remodeling factor with poorly understood function in the developing or adult brain. In human, *CHD2* haploinsufficiency is associated with intellectual disability, a variety of catastrophic childhood epilepsies, autism spectrum disorder and photosensitivity (Neale et al., 2012; Rauch et al., 2012; Chénier et al., 2014; Galizia et al., 2015), with large phenotypic variability among affected individuals. In mice, heterozygous deletion of *Chd2* results in histological abnormalities of heart, muscle, lung, liver, kidney, spleen and bone (Marfella et al., 2006; Marfella et al., 2008; Harada et al., 2012; Kulkarni et al., 2008). Initial studies in brain indicate *Chd2* knockdown during the peak of embryonic neurogenesis promotes production of neurons from neural progenitors, possibly depleting the precursor pool (Shen et al., 2015). However, unlike other CHD family members in which recent progress using animal models has led to important mechanistic insights about behavioral phenotypes and cellular pathways (Durak et al., 2016; Katayama et al., 2016; Gompers et al., 2017; Platt et al., 2017), there is essentially nothing known about brain defects that arise as a consequence of *Chd2* haploinsufficiency.

Understanding how mutations in chromatin remodeling genes impact brain function may reveal new opportunities for targeted therapies. This led us to generate a *Chd2* mutant mouse line and investigate the effect of *Chd2* haploinsufficiency on the developing and mature mouse brain. Our findings support the hypothesis that *Chd2* has a critical function in forebrain neurogenesis *in vivo*, and the generation of GABAergic interneurons in particular. We also found evidence of a functional role for *Chd2* in cortical circuit physiology and long-term spatial memory.

Results

CHD2 is expressed in neurons and oligodendrocytes

We first determined the expression profile of CHD2 in wild-type (WT) C57BL/6J mice at P30 (n = 6 mice) (Figure 1). Immunofluorescence experiments revealed CHD2 was widely expressed throughout the young-adult mouse brain, with especially strong expression in olfactory bulb, neocortex, hippocampus and cerebellum (Figure S1A, B). These observations are consistent with RNA expression patterns of *Chd2* detected by *in situ* hybridization (Gene Paint; https://gp3.mpg.de/results/chd2). To determine whether CHD2 expression was limited to a specific brain cell type, we further evaluated coronal sections from hippocampus of P30 WT mice (n = 11 mice). We found CHD2 co-localized in nearly all mature neurons (NEUN-

positive, 99.8 ± 0.1%), GABAergic interneurons (GAD67-positive, 97.7 ± 0.39%) and oligodendrocytes (OLIG2-positive, 97.6 ± 0.95%). Conversely, CHD2 was not expressed in the majority of GFAP-positive astrocytes (0.4 ± 0.4%) (Figure 1A, B). CHD2 co-localized with DAPI, consistent with its role in chromatin regulation (Figure S1C).

Generation of *Chd2*$^{+/-}$ mice

In human, *CHD2* mutations are typically loss of function (Carvill et al., 2015). To establish a mouse line with a heterozygous loss of function mutation in *Chd2* (i.e., *Chd2*$^{+/-}$ mice), we crossed transgenic mice containing loxP-flanked exon 3 of *Chd2* (i.e., Chd2$^{tm1c(EUCOMM)Hmgu}$ mice) with a b-actin Cre line (Figure 1C; Figure S1D-F). Mice with heterozygous deletion in *Chd2* showed approximately half the expression of CHD2 protein in brain as compared to WT littermates (Figure 1D, E). *Chd2*$^{+/-}$ mice of both sexes were viable and fertile but had reduced body weight compared to WT littermates (Male: [WT: 18.5 ± 0.8 g, n = 17 mice, *Chd2*$^{+/-}$: 16.2 ± 0.9 g, n = 23 mice; two-tailed t test; p = 0.001] Female: [WT: 16.4 ± 0.4 g, n = 22 mice, *Chd2*$^{+/-}$: 14.2 ± 0.7 g, n = 22 mice; two-tailed t test; p = 0.0004]) (Figure 1F). *Chd2*$^{+/-}$ mice also exhibited mild lordokyphosis by 2 months of age (Figure S1H). This phenotype was not apparent in WT littermates and is consistent with reports of scoliosis in humans with *Chd2* mutations (Chénier et al., 2014; Kulkarni et al., 2008).

We first asked whether a reduction in *Chd2* disrupts cytoarchitecture of the cortex. Analysis of the layer-specific markers BRN2 (layer II/III), CTIP2 (layer V and VI) and DAPI revealed no gross alterations to lamination at P30 (Figure 1G-I), and analysis of NEUN immunostaining showed no obvious laminar disorganization in somatosensory cortex or hippocampus (Figure S1I). No significant differences were detected in the thickness of somatosensory neocortex or dorsal hippocampus between genotypes (Figure 1H; Figure S1J). Likewise, we did not observe any differences in the width of the granule cell or CA1 pyramidal cell layers within hippocampus of *Chd2*$^{+/-}$ mice compared to WT littermates (Figure 1I; Figure S1K). Finally, we evaluated WT and *Chd2*$^{+/-}$ mice for cellular phenotypes of epilepsy in dentate gyrus. Analysis of Timm's staining revealed no mossy fiber sprouting into the inner molecular layer of the dentate gyrus (Mann-Whitney rank sum test, p=1.00, U-statistic = 162.00) (Figure S1L). We also found no change in the intensity of GFAP immunostaining or density of GFAP+ cells between genotypes (Figure S1M-P). Hence, our results show *Chd2* haploinsufficiency does not substantially disrupt cortical cytoarchitecture.

Reduced numbers of GABAergic interneurons in *Chd2*$^{+/-}$ mice

Because CHD2 was co-expressed with nearly all GABAergic interneurons, we asked whether numbers of individual GABA cell populations were altered in *Chd2*$^{+/-}$ mice. At P30, we found ~20% decrease in the density of GAD67-expressing cells in somatosensory cortex (WT: 302.3 ± 12.2 GAD67+ cells/mm^2, *Chd2*$^{+/-}$: 239.8 ± 11.3 GAD67+ cells/mm^2; n= 6 mice per genotype, p=0.03) and hippocampus CA1 (WT: 175.6 ± 5.9 GAD67+ cells/mm^2, n=5 mice; *Chd2*$^{+/-}$: 140.8 ± 2.8 GAD67+ cells/mm^2, n=6 mice; p=0.0003) (Figure 2). We also found ~10% decrease in the density of NEUN+/GAD67- cells (putative excitatory neurons) in somatosensory cortex (WT: 1,938 ± 45 cells/mm^2, *Chd2*$^{+/-}$: 1,791 ± 17 cells/mm^2; n= 4 mice per genotype, p=0.03) (Figure S2), suggesting *Chd2*$^{+/-}$ does not

selectively alter interneuron number, but no change was found in hippocampus CA1 (WT: 4,235 ± 205 cells/mm^2, *Chd2*$^{+/}$: 4,534 ± 192 cells/mm^2; n= 4 mice per genotype, p=0.3). Immunostaining analysis for GABAergic subtypes revealed decreased density of cells expressing parvalbumin (PV; 15% decrease in somatosensory cortex and 22% in CA1), somatostatin (SST; 11% decrease in somatosensory cortex and 31% in CA1) and reelin (12% decrease in CA1) (Figure 2). The density of cells expressing calretinin (CR) or vasoactive intestinal peptide (VIP) was not significantly different between genotypes.

One hypothesis that could explain fewer GABA neurons in *Chd2*$^{+/-}$ mutants is that *Chd2*$^{+/-}$ may favor the production of oligodendrocytes over interneurons, which derive from the same progenitor regions of the ventral telencephalon (Petryniak et al., 2007). To test this, we quantified the number of OLIG2+ cells at P30. However, we found no difference in OLIG2+ cell densities in somatosensory cortex (WT: 659.2 ± 33.5 cells/mm^2; *Chd2*$^{+/-}$: 662.7 ± 26.1 cells/mm^2; n=4 mice per genotype; p=0.94) or hippocampus CA1 (WT: 522.8 ± 10.5 cells/mm^2, n=4 mice; *Chd2*$^{+/-}$: 513.8 ± 25.0 cells/mm^2, n=3 mice; p=0.45) (Figure S3). Thus, decreases in interneuron density are unlikely due to increases in oligodendrogenesis in *Chd2*$^{+/-}$ mice.

Chd2$^{+/-}$ disrupts cell proliferation in the developing forebrain

Interneuron density in the adult nervous system is largely determined by the size of the precursor pool in the embryo (Southwell et al., 2012). To investigate whether *Chd2* has a role in GABAergic neurogenesis, we crossed *Chd2*$^{+/-}$ mice with a GAD67-GFP knock-in reporter labeling nearly all GABAergic interneurons (Tamamaki et al., 2003). CHD2 expression was observed throughout the embryonic brain of WT mice at E14.5 (n= 12 mice) (Figure 3A-C). In dorsal telencephalon, and in agreement with a previous report (Shen et al., 2015), CHD2 was expressed at the highest levels in the cortical plate, where it co-localized with the majority of TBR1+ cells, as well as the ventricular zone (VZ) and subventricular zone (SVZ), where CHD2 co-localized with KI67+ mitotically active precursors and PAX6+ radial glia (Figure 3A; Figure S4). In contrast, CHD2 expression was low or absent in the intermediate zone (IZ) and marginal zone (MZ) at this stage, and rarely overlapped with TBR2+ intermediate progenitors. In ventral telencephalon, CHD2 was expressed in the medial and caudal ganglionic eminence (MGE and CGE), progenitor domains that generate nearly all cortical GABAergic interneurons (Figure 3B, C; Figures S4). At this stage CHD2 strongly co-localized with KI67 and NKX2.1, but only partially co-localized GAD67-GFP+ cells in MGE. CHD2 was not detected in tangentially migrating interneurons in neocortex (Figure 3A). By demonstrating progenitor domain-specific expression of CHD2 during cortical development, our results suggest CHD2 plays a role in cell proliferation, terminal differentiation and maturation of cortical principal neurons and GABAergic interneurons.

To determine whether forebrain precursors were altered by *Chd2*$^{+/-}$, we performed a series of immunostaining studies at E14.5. In cortex, we found ~35% decrease in the density of KI67-expressing cells in VZ/SVZ of *Chd2*$^{+/-}$ mice (WT: 8,087.5 ± 934.8 cells / mm^2, n= 4 mice; *Chd2*$^{+/-}$ 5,150 ± 180.3 cells / mm^2; n=3 mice; p=0.04) (Figure 3D, E). In MGE, we also observed a ~35% decrease in the density of KI67-expressing cells in VZ/SVZ of *Chd2*$^{+/-}$ mice (WT: 8,910.5 ± 279.5 cells / mm^2, n= 5 mice; *Chd2*$^{+/-}$: 7,108.3 ± 361.2 cells /

mm^2; n= 3 mice; p=0.04). Further analysis at E14.5 revealed a subsequent decrease in NKX2.1-expressing progenitors in MGE (WT: 17,929.2 ± 717.2 cells / mm^2, n= 6 mice; *Chd2*$^{+/-}$: 15,000 ± 365.5 cells / mm^2, n= 5mice; p=0.008) and reduced density of GAD67-GFP+ neurons in cortex of *Chd2*$^{+/-}$ mice, as compared to WT littermates (WT: 3,122.5 ± 162.9 cells / mm^2, n= 4 mice; *Chd2*$^{+/-}$: 2,450.5 ± 39.9 cells / mm^2, n= 6 mice; p=0.02) (Figure 3F-I). Finally, we asked whether *Chd2*$^{+/-}$ altered caspase-3 mediated interneuron cell death, which peaks around P7 in mice (Southwell et al., 2012). At P7, we found a decrease in the density of GAD67-GFP+ cells in somatosensory cortex (WT: 781.1 ± 50.78 cells / mm^2; *Chd2*$^{+/-}$: 643.3 ± 40.21 cells / mm^2; n= 5 mice per genotype; p=0.04), but density of cells expressing caspase-3 was not different between genotypes (Figure 3J-L). We conclude that *Chd2* haploinsufficiency disrupts cell proliferation and neurogenesis in the developing forebrain, but not developmentally-programmed cell death.

Differential gene expression in *Chd2*$^{+/-}$ mice

As a chromatin modifier, *Chd2* likely plays an important role in global transcriptional regulation, but its exact function in brain is unknown (Marfella et al., 2007; Tyagi et al., 2016). Having established that CHD2 is expressed in both the embryonic forebrain and mature neurons, we next sought to identify transcriptional changes resulting from *Chd2* haploinsufficiency in an unbiased way. To do this, we performed polyA+ RNA-sequencing on tissue micro-dissected from neocortex and MGE of developing embryos at E13.5 as well as hippocampus in adult mice at P45 (Figure 4A). We tested for differential expression (DE) across 24,062 genes expressed in our data sets in 9 WT mice and 7 *Chd2*$^{+/-}$ littermates. At significance cutoffs corresponding to Benjamini and Hochberg adjusted P-value < 0.1, we found 44 (E13.5 MGE), 14 (E13.5 neocortex) and 652 (P45 hippocampus) DE genes in *Chd2*$^{+/-}$ mice (Figure 4B, Table S2). In addition, we further validated expression changes of a randomly selected group of DE genes via qRT-PCR (Figure 4C). In all three groups, *Chd2* was down-regulated (E13.5 MGE: $2^{-\Delta\Delta Ct} = 0.32$, P = 0.04; E13.5 Neocortex: $2^{-\Delta\Delta Ct} = 0.36$, P = 0.04; P45 Hippocampus: $2^{-\Delta\Delta Ct} = 0.62$, P = 0.04) (Figure 4C).

Analysis of Gene Ontology (GO) terms revealed brain region-specific dysregulation in *Chd2*$^{+/-}$mice compared to WT littermates. For this analysis, we expanded the list of DE genes to a significance cutoff of P-value < 0.05 for E13.5 datasets, which increased sample sizes to 1416 (E13.5 neocortex) and 622 (E13.5 MGE) DE genes; adjusted P-value < 0.1 (P < 0.0045) was used for P45 hippocampus samples. At E13.5, DE genes showed strong enrichment for annotations associated with nervous system development, neuron differentiation and neurogenesis (Table S3). Similar enrichment was observed for DE genes in hippocampus at P45, with numerous additional annotations associated with synapse organization, transcriptional regulation and behavior (Figure 4D; Table S3). In particular, we found robust differential expression of transcription factors related to forebrain neurogenesis (e.g., *Neurod2, Neurog2* and *Sox4*), RNA silencers (e.g., *Ago2*), global regulators of the epigenome (e.g., *Ep300* and *Smarca4*), cell adhesion molecules (e.g., *Cdh4* and *Pcdh17*) and ion channels (e.g., *Kcna4* and *Cacnb1*). However, most striking was the broad range of up- and down-regulated genes related to neuronal activity and synaptic plasticity in P45 hippocampus (Table S4). Of note, the majority of differentially expressed synaptic molecules are involved in glutamatergic synaptic function (e.g., *Grina*, *Shank2*, *Homer1*). In

agreement with previous reports that chromatin remodeling proteins act as regulators of Wnt signaling pathways (Kwan et al., 2016), we found downregulation of numerous Wnt pathway genes in *Chd2*$^{+/-}$ mice, such as *Wnt7a*, *Wnt7b*, *Fzd1*, *Lrp1*, *Ctnnd2*, *Apc2*, and *Apcdd1*. However, we noted little overlap in the specific DE genes found in our data compared to prior studies on *Chd8* mutation (Durak et al., 2016; Katayama et al., 2016; Gompers et al., 2017; Platt et al., 2017), suggesting CHD subfamily members have distinct functional roles in brain.

A number of chromatin remodelers, including *Chd2*, have been implicated in human neurodevelopmental disorders (Marfella et al., 2007; Carvill et al., 2015; Kwan et al., 2016; Tyagi et al., 2016; Mastrototaro et al., 2017; Sokpor et al., 2017). Therefore, we next asked whether *Chd2*$^{+/-}$ altered genes implicated in human disease. Analysis of Disease Ontology (DO) terms identified DE genes for annotations associated with epilepsy and autism spectrum disorders as well as numerous other neurological diseases, such as mental health disorders, congenital disease and cancer (Figure 4E; Table S5). In particular, we found 123 DE genes associated with intellectual disability (e.g., *Cacna1g, Ctnnd2* and *Hexa*), childhood epilepsy (e.g., *Hdac4, Pcdh19, Reln* and *Slc6a1*) and/or autism spectrum disorders (e.g., *Grin2b, Ktm2a* and *Shank2*) (Figure 4F), some of which are strong candidate “risk” genes while others are relatively uncharacterized. Altogether, our results indicate *Chd2*$^{+/-}$ leads to a broad dysregulation of genes involved in neurogenesis, synapse organization and disease-related pathways.

Chd2$^{+/-}$ disrupts excitatory and inhibitory synaptic function in hippocampus

The observation that Chd2$^{+/-}$ drastically alters genes involved in synapse organization led us to investigate whether there is a change in neuronal or synaptic function in Chd2$^{+/-}$ mice. To do this, we examined electrophysiological properties of CA1 pyramidal neurons at P30–35 using patch-clamp recordings in acute hippocampal slices (Figure 5). Compared to WT animals, pyramidal neurons from *Chd2*$^{+/-}$ mice showed an increase in action potential firing at current injections exceeding 100pA (genotype: $F_{(1, 25)} = 2.06$; $p = 0.164$), current step: $F_{(1,16)} = 279.22$; $p < 0.001$; genotype by current step interaction: $F_{(1,16)} = 4.53$; $p < 0.001$; n= 13 cells from 3 WT mice, n= 14 cells from 4 *Chd2*$^{+/-}$ mice; two-way repeated-measures ANOVA) (Figure 5A, B). Consistent with greater firing capacity in CA1 pyramidal neurons, we also found a significant decrease in spike adaptation at 2x spike threshold in recorded neurons (WT: 1.61 ± 0.13, *Chd2*$^{+/-}$: 1.3 ± 0.07; p = 0.03; Mann Whitney U), but all other intrinsic electrophysiological properties examined were not significantly different between treatment groups (Figure 5C; Table S6).

Next, we examined miniature excitatory and inhibitory synaptic inputs onto CA1 pyramidal neurons in the presence of 1μM tetrodotoxin (TTX). Compared to WT littermates, pyramidal neurons in *Chd2*$^{+/-}$ mice exhibited a significant increase in miniature excitatory postsynaptic current (mEPSC) amplitudes, without a change in event frequency (n = 14 cells from 4 WT mice, n= 16 cells from 4 *Chd2*$^{+/-}$ mice; Figure 5D-F). This was accompanied by significantly faster decay kinetics in *Chd2*$^{+/-}$ mice; 10–90% rise time was not different between genotypes. (Figure 5G-I). In contrast, *Chd2*$^{+/-}$ mice exhibited a decrease in miniature inhibitory postsynaptic current (mIPSC) frequency, without a change in mIPSC

amplitude or event kinetics (n = 20 cells from 3 WT mice, n= 21 cells from 3 *Chd2*$^{+/-}$ mice; Figure 5J-O). Fewer mIPSCs onto CA1 pyramidal neurons could be explained by a loss of GABAergic synapses or a change in GABA release probability in *Chd2*$^{+/-}$ mice (Hirsch et al., 1999). Therefore, we evaluated evoked IPSC responses to paired stimuli applied to stratum radiatum, a commonly used measure of presynaptic short-term plasticity. However, we did not observe a change in paired-pulse ratio (PPR) of evoked-IPSCs between genotypes, suggesting that presynaptic GABA release is unaltered in *Chd2*$^{+/-}$ mice (Figure S5). Taken together, our findings indicate *Chd2*$^{+/-}$ alters neuronal excitability and has differential effects on glutamatergic versus GABAergic synaptic transmission in hippocampus.

Chd2$^{+/-}$ mice exhibit changes in cortical rhythmogenesis

A change in the normal balance between excitation and inhibition has the capacity to disrupt naturally occurring oscillations in the brain. Thus, we implanted electroencephalogram (EEG) electrodes into somatosensory neocortex of freely behaving *Chd2*$^{+/-}$ mice and WT littermates (n = 5 mice per genotype) and recorded intracranial EEG >1 wk later at P40–65 (Figure 6). Analyses of the local field potential revealed clear episodes of each frequency band in WT mice and *Chd2*$^{+/-}$ littermates, indicating these rhythms remain intact in the mutants (Figure 6A,B). We found that *Chd2*$^{+/-}$ mice exhibited a significant increase in the alpha (8–13Hz) and gamma (30–70Hz) frequency ranges compared to WT littermates (Figure 6C), suggesting cortical synchrony is increased by *Chd2* haploinsufficiency. Notably, elevations in resting alpha or gamma power have been observed in human epilepsies (Willoughby et al., 2003; Vaudano et al., 2017), autism spectrum disorders (Orekhova et al., 2007; Cornew et al., 2013) and mouse models featuring deficits in interneuron function (Korotkova et al., 2010; Carlén et al., 2012; Del Pino et al., 2013; Howard et al., 2013; Cho et al., 2015). Examination of the mean normalized power spectra for all other frequency ranges revealed no differences between genotypes (Figure 6C). Further analysis revealed differences in cross-cortical coherence (a measure of phase and amplitude synchrony between hemispheres) in delta, theta and gamma frequency ranges (Figure 6D). Next, we performed 24h/7d EEG monitoring to test whether *Chd2*$^{+/-}$ mice develop spontaneous electrographic seizures. In 7 days of continuous monitoring at P40-P65, we did not observe any overt convulsive seizures in WT or *Chd2*$^{+/-}$ mice (n=6 mice per genotype). Altogether, these findings indicate *Chd2* haploinsufficiency leads to a dysregulation of neural oscillations and synchrony in cortex.

Chd2$^{+/-}$ disrupts long-term memory

Memory requires changes in neuronal gene expression that are coordinated, at least in part, by epigenetic mechanisms and chromatin regulation (Levenson et al., 2013; Vogel-Ciernia et al., 2013a; Mews et al., 2017). To assess long-term memory in *Chd2*$^{+/-}$ mice, we used the well-characterized object-location and recognition memory paradigms (Vogel-Ciernia et al., 2013b) (Figure 7; Figure S6A, B). During a 10 minute habituation phase in the open field arena, the total distance traveled was not different between groups, but *Chd2*$^{+/-}$ mice spent more time in the center region of the arena, as compared to wild-type littermates (Figure S6C-E; Table S7). In the object location task, WT mice exhibited increased exploration of the object that had been moved (Figure 7A-C). In contrast, *Chd2*$^{+/-}$ mice explored both

objects equally (Figure 7A-C) and displayed a significantly lower discrimination index compared to WT controls (Figure 7B, C). Similarly, in the object recognition task, WT mice exhibited increased exploration of the novel object (Figure 7D-F), but *Chd2*$^{+/-}$ mice explored both objects equally (Figure 7D-F) and displayed a significantly lower discrimination index compared to WT controls (Figure 7E, F). There was no difference in the time spent exploring the objects (Figure S6F, G), suggesting the poor performance of *Chd2*$^{+/-}$ mice was not due to disinterest in the objects, and locomotor activity during training and test phases was comparable between groups (Figure S6E). *Chd2*-conditional-mutant mice with *Chd2* haploinsufficiency only in inhibitory interneurons (Nkx2.1-Cre; Chd2$^{loxP/+}$; Ai14-tdTomato mice) showed similar impairments in interneuron density and memory behaviors (Figure S7). We conclude that *Chd2*$^{+/-}$ mice exhibit severe deficits in long-term spatial and recognition memory, and this is due, at least in part, to a reduction in the number of cortical interneurons.

MGE transplantation rescues spatial memory problems in *Chd2*$^{+/-}$ mice

In hippocampus, deficits in interneuron number or function have been implicated in a wide range of cognitive disorders, such as Alzheimer's disease (Satoh et al., 1991), intellectual disability (Opperman et al., 2017) and epilepsy (de Lanerolle et al., 1989). With this in mind, we next asked whether transplantation of inhibitory interneurons is sufficient to "rescue" memory deficits observed in *Chd2*$^{+/-}$ animals. To do this, MGE progenitors were obtained from E13.5 β-actin:GFP donor mice, and 5×10^4 cells were injected bilaterally into hippocampus of neonatal recipients at postnatal day 5 (Figure 8A). We performed polyA+ RNA-sequencing and DE analysis between MGE and neocortex micro-dissected from E13.5 embryos to confirm the grafted cells expressed genes highly enriched in MGE-derived progenitors (Olig2, Dlx5, Lhx6, Pou3f4 and Gad1) (Figure 8B; Table S8). By 45 days after transplant (DAT), MGE-GFP cells migrated away from the injection and were dispersed throughout hippocampal subfields (n=3 mice per genotype) (Figure 8C; Figure S8A, B). GFP-labeled cells expressed the interneuron markers PV (WT: 18 ± 4%; *Chd2*$^{+/-}$: 24 ± 6%) and SST (WT: 35 ± 6%; *Chd2*$^{+/-}$: 28 ± 2%), but did not express VIP (<1% both genotypes) (Figure 8D). No differences in marker expression were detected between genotypes (Figure S8C). Finally, we assessed the effect of MGE transplantation on long-term memory. Replication with a second, independent cohort of WT and *Chd2*$^{+/-}$ mice showed *Chd2*$^{+/-}$ mutants had deficits in both object location and recognition memory tasks (Figure 8E, F). Chd2$^{+/-}$ mice that received MGE grafts exhibited improvement in the novel object location task, but not the object recognition assay; MGE transplantation had no effect on memory in WT animals. These findings suggest increasing the number of inhibitory interneurons is sufficient to restore deficits in long-term spatial memory of *Chd2*$^{+/-}$ mice, but recognition memory remains impaired.

Discussion

Our results provide the first comprehensive molecular and physiological analysis of *Chd2* haploinsufficiency. Using a new mouse model of *Chd2* mutation, we found alterations in neural progenitor proliferation in the embryo as well as defects in synaptic transmission, cortical synchrony and hippocampal-dependent memory behavior in adult mice. In

agreement with these findings, transcriptome analysis revealed broad changes in the expression of genes involved in chromatin regulation, neurogenesis and synaptic transmission. Transplantation of MGE-derived interneurons rescued deficits in interneuron number and hippocampal-dependent spatial memory. While *Chd2*$^{+/-}$ mice exhibited changes in excitation-inhibition activity at the synaptic and network levels, we did not observe overt spontaneous seizures. However, many individuals with *CHD2* haploinsufficiency also do not have epilepsy, and *CHD2* mutations have been identified in patients with autism (O'Roak et al., 2014) and intellectual disability without seizures (Hamdan et al., 2014). Overall, these observations demonstrate *Chd2*$^{+/-}$ mice reproduce many, but not all, of the key behavioral phenotypes observed in humans with *Chd2* mutations. Careful phenotyping of additional patients will help better define the phenotypic spectrum of this disorder in human.

An emerging literature on chromatin biology is revealing that genes encoding CHD proteins are critical regulators of brain development, from cell proliferation to differentiation (Marfella et al., 2006; Marfella et al., 2007; Marfella et al., 2008; Shen et al., 2015; Durak et al., 2016; Katayama et al., 2016; Kwan et al., 2016; Tyagi et al., 2016; Mastrototaro et al., 2017; Sokpor et al., 2017; Gompers et al., 2017; Platt et al., 2017; Meganathan et al., 2017). Whereas most studies have focused on cell signaling pathways and/or behavioral phenotypes, our results demonstrate a potential link between chromatin regulation and behavior, via alterations in synaptic transmission and cortical network synchrony. Though CHD2 is located in cell nuclei, we found that *Chd2* mutations perturb neural circuit function in at least two distinct ways in the mature brain depending on the system. In glutamatergic circuits, which have a prominent role in hippocampal-dependent learning and memory, we observed transcriptional changes related to pre- and post-synaptic domains that lead to an increase in glutamatergic transmission and faster event kinetics. In contrast, reduced progenitor proliferation predominates in GABAergic circuits, and this leads to fewer inhibitory interneurons and a reduction in synaptic inhibition in hippocampus. The balance of excitatory-inhibitory synaptic interactions is essential for the formation of neural oscillations (Atallah et al., 2009) and memory (Lim et al., 2013), deficits we observed in *Chd2*$^{+/-}$ mice.

Early insight into the function of CHD2 in brain indicated expression of repressor element 1-silencing transcription factor (REST), a master regulator of neuronal development, was positively correlated with CHD2 (Shen et al., 2015), which may lead to alterations in radial glia self-renewal and neurogenesis when disrupted. Our RNA-sequencing analysis did not confirm downregulation of REST in any brain region examined. This may be related to differences between *in utero* knockdown via *Chd2* shRNA delivery to embryonic ventricles versus transgenic mutation; transcriptional changes in REST following *in utero* knockdown of *Chd8* also could not be replicated by germline mutation (Durak et al., 2016; Katayama et al., 2016; Gompers et al., 2017; Platt et al., 2017). One of the main differences between *Chd2*$^{+/-}$ versus other mouse models of *Chd* mutation (e.g., *Chd8*$^{+/-}$) is that *Chd2*$^{+/-}$ mice have a severe interneuron deficit whereas no such deficit has been reported in any of the mouse models of *Chd8*$^{+/-}$ (Durak et al., 2016; Katayama et al., 2016; Gompers et al., 2017; Platt et al., 2017). Indeed, a recent report suggests *Chd2* may co-associate with Nkx2.1 at *cis*-regulatory elements to regulate gene expression programs in presumptive interneurons derived from human embryonic stem-cells (Meganathan et al., 2017). We found evidence of

altered neurogenesis in mice, notably a reduction in precursor pools of both excitatory and inhibitory neurons in the embryonic forebrain. Nevertheless, a clear disruption of cortical cytoarchitecture was not apparent in mutant animals, consistent with the absence of structural brain abnormalities among many people with *CHD2* mutations (Chénier et al., 2014). It is possible that *Chd2* also plays a role in the development of non-neuronal cell types, such as oligodendrocytes or astrocytes. Our experiments primarily focused on analysis of neural progenitors, because we did not observe co-localization of CHD2 in GFAP+ cells or a change in OLIG2+ cell densities in *Chd2*$^{+/-}$ mice. A detailed and direct analysis of individual neuronal and glial cell types should clarify the developmental source or molecular mechanisms driving *Chd2*-related pathology. Nevertheless, our findings suggest that cell-type specification and migration of neural progenitors into the cortex remains largely intact in *Chd2*$^{+/-}$ mice.

Hundreds of rare gene mutations are now associated with neurodevelopmental disorders, many of which have devastating behavioral consequences that cannot be managed with available treatment options. Although discovery of new disease-associated gene mutations has been expanding rapidly, a major challenge in the field is to identify mechanisms underlying each of these rare disorders so that new, disease-specific therapies can be developed. Our results suggest interventions targeting cell proliferation and/or synaptic signaling may be particularly promising therapeutic candidates in *Chd2* haploinsufficiency. Given DO analysis revealed 16 DE genes associated with obesity and the strong link between altered metabolism and seizures (Sharfman, 2015), metabolic pathways may be a promising disease target, as well. Indeed, some patients with *CHD2* mutation found improvement with ketogenic diet (Chd2 Support and Research Group; https://www.facebook.com/groups/1462485137354985/), and there is evidence of improved memory performance with this treatment in aging mice (Newman et al., 2017). While further studies of the neuroanatomical and physiological changes associated with *Chd2* mutations are necessary before precise therapies can be designed and translated to the clinic, our results are an important step toward understanding how mutations in *Chd2* impact brain development and function.

STAR★Methods

Contact for Reagent and Resource Sharing

Further information and requests for resources and reagents should be directed to and will be fulfilled by the Lead Contact, Robert F Hunt (robert.hunt@uci.edu).

Experimental Model and Subject Details

Mice—Mice were maintained in standard housing conditions on a 12h light/dark cycle with food and water provided *ad libitum*. All protocols and procedures followed the guidelines of the University Laboratory Animal Resources at the University of California, Irvine and adhered to National Institutes of Health Guidelines for the Care and Use of Laboratory Animals. To generate Chd2-flox mice (i.e., Chd2$^{tm1c(EUCOMM)Hmgu}$ mice), we obtained sperm with tm1c conditional allele from The Centre for Phenogenomics and re-derived the transgenic line on a C57BL/6J background (Jackson Laboratories cat. no. 000664) at the

UCI Transgenic Mouse Facility. A full description of the targeting of *Chd2* can be found at International Mouse Phenotyping Consortium (https://www.mousephenotype.org/data/genes/MGI:2448567). Chd2-flox mice were then crossed for three generations to WT C57BL/6J mice and the offspring of the third generation was crossed to an ACTB-Cre line (Jackson Laboratories cat. no. 019099) to generate $Chd2^{+/-}$mice. In some experiments, Chd2-flox mice were mated with a Nkx2.1-Cre (Jackson Laboratories cat. no. 008661), an Ai14 tdTomato reporter (Jackson Laboratories cat. no. 007908) or a hemizygous glutamic acid decarboxylase - enhanced green fluorescence protein (GAD67-GFP) knock-in line maintained on a CD-1 background (Tamamaki et al., 2003). To obtain embryos for MGE transplantation, male β-actin:GFP mice (Jackson Laboratories cat. no. 006567) were crossed to CD-1 females (Charles River, cat no. 022). Experiments were performed on male and female littermates between E14.5 and P75.

Method Details

Experimental design—Experiments were performed on male and female littermates between E14.5 and P75. Animals were randomly allocated to experimental groups, and the experimenter was blinded to genotype of the animals until the experiment was complete. No data or animals were excluded from analysis. Memory behavior assays were replicated using a separate, independent cohort of WT and $Chd2^{+/-}$ littermates. No other replication studies were performed.

Western Blot—Western blot was performed on P30 mice as previously described (Luijsterburg et al., 2016). Nuclear protein extracts from whole brain were prepared by homogenizing the tissue in subcellular fractionation buffer (20 mM HEPES (pH7.4), 74.55 mM KCl, 95.21 mM MgCl2, 292.24 mM EDTA, 380.35 mM EGTA, 1 mM DTT and 1x Protease inhibitor cocktail). Proteins were separated by sodium dodecyl sulfate polyacrylamide gel electrophoresis (SDS-PAGE) and transferred to PVDF membranes. Protein expression was analyzed by immunoblotting. Primary antibodies and dilutions are provided in the Key Resources table. Secondary antibodies were IRDye 800CW (LI-COR) and CF770 (Biotium). Gels were imaged and quantified using a LI-COR Odyssey infrared imaging scanning system.

Immunostaining—Mice were transcardially perfused with 4% paraformaldehyde (PFA) and free-floating vibratome sections (50 μm) were processed using standard immunostaining procedures (Hunt et al., 2013). For E14.5 embryos, brains were dissected and drop-fixed overnight in 4% PFA. For Pax6, Ki67, and Tbr2 staining, sections were pretreated with an antigen unmasking solution (10mM Sodium Citrate, pH 6.0) for 60 minutes at room temperature. All antibodies have been previously used for immunostaining analysis in brain. Primary antibodies and dilutions are provided in the Key Resources table. Secondary antibodies were: Alexa 488, Alexa 561, Alexa 594 and Alexa 647 (Invitrogen). Sections were then mounted on charged slides (Superfrost plus; Fisher Scientific) with Vectasheild that contained DAPI or Aqua Mount. Images were obtained with a Leica DM6 epifluorescence microscope or an Olympus FV3000 laser-scanning confocal microscope. Brightness and contrast were adjusted manually using Adobe Photoshop; z-stacks were generated using Olympus, Leica or Helicon Focus 6 software.

Cell quantification—Fluorescently labeled sections (50 μm) were imaged using a Leica DM6 microscope with a x10 or x20 objective or Olympus FV3000 confocal microscope with a x20 or x40 objective and counted using ImageJ, as described previously (Hunt et al., 2013). All cells that expressed a subtype maker were counted in every sixth coronal section (that is, 300 μm apart). Four to six sections were analyzed per animal and the values averaged to obtain a mean cell density (cells / mm^2). Intensity measurements were analyzed within regions of interest and a range of threshold limit was applied using ImageJ according to a previous protocol (Jensen, 2013).

Timm's Staining—Animals were perfused transcardially with 0.37% sodium sulfide solution in 0.1 M NaHPO4, followed by 4% PFA and stored overnight in 4% PFA solution. Brains were then sectioned at 50 μm on a vibratome and every sixth section mounted on charged slides (Superfrost Plus; Fisher Scientific). Sections were dried overnight and treated according to previous protocols using Timm's stain to reveal mossy fibers and Nissl counterstained with cresyl violet to visualize cell bodies (Tauck and Nadler, 1985; Hunt et al., 2009). To semi-quantitatively assess the presence or absence of mossy fiber sprouting into the inner molecular layer of the dentate gyrus, Timm scores from 0 (little to no sprouting) to 3 (robust mossy fiber sprouting) (Tauck and Nadler, 1985; Hunt et al., 2009) were assigned to six randomly chosen sections from the dorsal portion of the hippocampus and averaged for each animal. Images were taken with a Leica MZ10F stereoscope.

RNA sequencing—Total RNA was isolated from freshly dissected tissue using the Direct-zol RNAMiniPrep Plus kit (Zymo Research) according to the manufacturer instructions. RNA quantity and quality was then determined for each sample using NanoDrop (ThermoFisher), Qubit RNA BR Assay Kit (ThermoFisher), and a TapeStation (Agilent). Samples were then converted to cDNA using the NEBNext Ultra RNA Library Preparation Kit (NEB) with poly(A) selection. Paired-end sequencing was performed on the Illumina HiSeq 4000 platform by GENEWIZ Next Generation Sequencing facility (South Plainfield, NJ). Quality of the raw sequencing reads was accessed using FASTQC and adaptors were trimmed with Trimmomatic. Reads for each library (32.7 ± 4.6 million per replicate, n = 18 replicates) were then aligned using TopHat2 (version 2.1.1) and the mouse genome index mm10 generated from iGenome UCSC mm10 FASTQ genome sequence.

Differential expression analysis—Quantification and differential expression of the annotated mouse genes were performed using DESeq2 as previously described (Love et al., 2014) using three biological replicates for each dataset. Differences were considered statistically significant with Benjamini and Hochberg (BH) adjusted P-value <0.10 and P-values <0.05. GO analysis and functional classification were performed separately on up- or down-regulated genes using the R package *goseq* (Young et al., 2010), with corrected gene length and expressed genes as the background test set. Significance was set at Benjamini and Hochberg adjusted P-value < 0.1 or P-value <0.05. DO analysis of functional enrichment based on human diseases in the DisGeNET database (http://www.gisgenet.org/) was performed separately on up- or down-regulated genes using the R package *DOSE* (Yu et al., 2015) and expressed genes as the background test set. Heat maps and bubble plot were generated with the R packages *pheatmap* and *GOplot*. For disease gene plots in Figure 4F,

risk genes for epilepsy, intellectual disability and/or autism were determined based on the following databases: SFARI Human Gene Module (https://gene.sfari.org/database/human-gene), Citizens United Against Epilepsy (CURE) Foundation Epilepsy Genetics Initiative (https://www.cureepilepsy.org/egi), DECIPHER v9.17 (https://decipher.sanger.ac.uk) and ID Gene Database Project (http://gfuncpathdb.ucdenver.edu/iddrc/iddrc/home.php). We found a significant disruption in Tmem163 of *Chd2*$^{+/-}$ mice (Table S2), which is likely the result of Cre insertion into intron 4 of Tmem163 in the ACTB-Cre line (Cain-Hom et al., 2017). Since we analyzed three female and three male samples by chance for the comparison of WT and *Chd2*$^{+/-}$ MGE, we also found several sex-specific genes with significant and large changes (Table S2).

Quantitative (q) RT-PCR—Total RNA was extracted with Direct-zol RNA MiniPrep Plus (Zymo Research) and reverse-transcription performed using iScript cDNA Synthesis Kit (Bio-Rad) according to the manufacturer instructions. The resulting cDNA was subjected to qPCR analysis with the Applied Biosystems ViiA 7 Real-Time PCR System using SsoAdvanced Universal Inhibitor-Tolerant SYBR Green Supermix (Bio-Rad cat no. 1725016) and gene specific primers (Key Resources table). Reactions were repeated in triplicates. Relative expression levels were calculated using the the $2^{-\Delta\Delta CT}$ method using *Actb* as an endogenous control gene.

Slice electrophysiology—Coronal brain slices (300 μm thickness) were prepared from WT and *Chd2*$^{+/-}$ littermates at P30-P35. Slices were submerged in the recording chamber and continuously perfused with oxygenated ACSF (32 –34°C) containing (in mM): 124 NaCl, 3 KCl, 1.25 NaH_2PO_4-H_2O, 2 $MgSO_4$-$7H_2O$, 26 $NaHCO_3$, 10 dextrose, and 2 $CaCl_2$ (pH 7.2–7.4, 300–305 mOsm/kg). Whole-cell patch-clamp recordings were performed at x40 using an upright, fixed-stage microscope (Olympus BX51WI) equipped with infrared, differential interference contrast (IR-DIC) and epifluorescence optics. For current-clamp and voltage-clamp recordings of EPSCs, patch pipettes (3–5 M) were filled with an internal solution containing (in mM): 140 K^+ gluconate, 1 NaCl, 5 EGTA, 10 HEPES, 1 $MgCl_2$, 1 $CaCl_2$, 3 KOH, and 2 ATP, pH 7.25. For voltage-clamp recordings of IPSCs, patch pipettes (3–5 M) were filled with an internal solution containing (in mM): 140 CsCl, 11 EGTA, 10 HEPES, 1 MgCl2, 2 NaATP, 0.5 NaGTP and 1.25 QX-314, pH 7.2. Recordings were obtained with a Multiclamp 700B amplifier, filtered at 4 kHz, and recorded to pClamp 10.7 software (Clampfit; Axon Instruments). For current-clamp experiments, cells were held at −70 mV, and electrophysiological properties were measured in response to a series of long (1000 ms) hyperpolarizing and depolarizing current-injections (10 pA steps; range: −80 pA to 160 pA). Voltage-clamp recordings were examined at a holding potential of −70 mV. Glutamatergic currents were measured in the presence of 30uM bicuculine, GABAergic currents were measured in the presence of 1mM kynurenic acid and 1uM TTX was added to the bath to isolate miniature PSCs. A concentric bipolar stimulating electrode made of platinum–iridium wire (125 μm diameter; FHC) was used to apply paired stimuli to CA1 stratum radiatum (100 μs duration, 100ms interstimulus interval). Stimulus intensity was set at 1.5 x threshold, where threshold was defined as the stimulus required for evoking an IPSC in 50% of the trials. Ten consecutive responses were obtained at 0.1 Hz, averaged and the ratio of the amplitude of the second evoked IPSC to the first (eIPSC2/eIPSC1) was

calculated to obtain the paired-pulse ratio (PPR). Series resistance was uncompensated and monitored throughout the recordings. Data were only used for analysis if the series resistance remained <20 M and changed by ≤20% during the recordings. Recordings were not corrected for a liquid junction potential. Resting membrane potentials were measured immediately after breakthrough by temporarily removing the voltage clamp and monitoring voltage. Data analysis was performed using pClamp 10.7, MiniAnalysis 6.0.7 (Synaptosoft), Microsoft excel or Sigmaplot 13 programs. A 2 min sample recording per cell was used for measuring event frequency, amplitude, 10–90% rise time, and decay time constant. Events characterized by a typical fast rising phase and exponential decay phase were manually detected using MiniAnalysis. The threshold for event detection was currents with amplitudes greater than three times the root mean square (RMS) noise level.

Electroencephalography (EEG)—Male *Chd2*$^{+/-}$ mice and age-matched male WT littermates were housed together before and after EEG surgeries. Local field potential recordings were obtained at 2kHz using an EEG monitoring system (Pinnacle Technologies) as previously described (Hunt et al., 2013; Khoshkhoo et al., 2017). Briefly, mice were anesthetized with ketamine and xylazine (10 mg/kg and 1 mg/kg i.p.), and sterile, stainless steel screw recording electrodes were placed epidurally through burr holes in the skull using surface head–mount EEG hardware (Pinnacle Technologies). The EEG recording electrodes were implanted at (in millimeters relative to the bregma): −1.25AP, ±1.5ML; reference electrode was implanted at −5.0 AP, 0 ML (in cerebellum), and a ground electrode was implanted at −3.5 AP, −3.0 ML. Electrodes were cemented in place with a fast–acting adhesive and dental acrylic. Two wires were laid on the shoulder muscles for electromyographic (EMG) recording. Animals were allowed to recover for at least 7 days before experiments were initiated and then monitored for 7–10 days (24 h/day). EEG recordings for each mouse were visualized in 1 hour time windows and carefully inspected for any abnormal electrographic signals or seizures. This process was repeated twice for each animal. All analyses were performed using custom-written and built-in MATLAB (MathWorks, Inc.) functions. To generate EEG power plots, total EEG power for each frequency interval was calculated in 10 minute bins using the Matlab function bandpower and averaged over 1 hour intervals. Then, the output was normalized by the total area under the curve (for frequencies <100 Hz, excluding 59–61 Hz) for each mouse. To analyze changes in baseline power 60 hours of continuous EEG recording, hours 12 through 72, was included for each mouse in order reduce the effect of arousal and environmental noise in our analysis. Two-way ANOVA was used to assess the effect of genotype, frequency, and genotype-frequency on baseline EEG power followed by a Tukey-Kramer multiple comparisons test to compare EEG power for each frequency band. To assess inter-hemispheric synchronization in each frequency interval, coherence between the EEG signals from the two hemispheres was calculated using the MATLAB function mscohere in 10 min bins, and averaged over 1 hour. A total of 60 hours of continuous EEG recording was included in this analysis for each mouse. Two-way ANOVA was used to assess the effect of genotype, frequency, and genotype-frequency on inter-hemispheric coherence followed by a Tukey-Kramer multiple comparisons test to compare inter-hemispheric coherence in mutant and WT mice for each frequency band.

Object location and recognition memory assays.—Each object location task consisted of a habituation phase, training phase and testing phase and were performed according to a previous protocol (Vogel-Ciernia et al., 2013a, b). Mice were handled for 2–5 minutes on 5 consecutive days before testing. On day 1, animals were habituated individually to the open field arena. Mice were placed in the center of a 40 cm × 40 cm × 35 cm open field arena with a vertical marking strip for 10 min under dim overhead lighting conditions (45 lux). For the training session (day 2), two identical objects were placed in the open field, 1 cm from the back wall and mice were placed in the center of the opposite wall. Animals were allowed to explore each object for 10 minutes. The arena and objects were cleaned with 70% (v/v) EtOH (OLM) or 1% acetic acid (ORM) between trials. A retention test was performed 24 hours after the training session (day 3). For OLM, one object was placed in a different location. For ORM, one object was exchanged for a new object that was different in size, shape and texture. The objects used were Falcon™ 50mL conical centrifuge Tubes (Fisher, Cat no. 14–432-22) filled with beach sand, 3D printed cube and a 75mL glass flask. For detailed description of the experimental setups, schematics are shown in Figures S6A,B and S7C,E. All behavioral assays were conducted between 2pm and 6pm during the light phase of the light/dark cycle (lights off at 8pm; lights on at 8am). Mouse identities were coded, and all behaviors were performed using a video tracking system and analyzed using ANY-maze software by investigators who were blind to the genotype and treatment of the animals. A mouse was scored as exploring an object when its head was oriented toward the object within a distance of 1 cm or when the nose was touching the object. The relative exploration time was recorded and expressed by a discrimination index ($DI = [t_{novel} - t_{familiar}]/[t_{novel} + t_{familiar}] \times 100$) where t represents time. Mean exploration times were calculated and the discrimination indexes between treatment groups were compared. To diminish bias, control and mutant littermates were evaluated on the same day in the same arena, and the location of the novel object was counterbalanced across experiments and groups.

MGE transplantation—Ventricular and subventricular layers of the MGE were harvested from E13.5 GFP+ embryos. The time point at which the sperm plug was detected was considered E0.5. Embryonic MGE explants were dissected in Leibovitz L-15 medium, mechanically dissociated by repeated pipetting and concentrated by centrifugation (3 min at 1,000 *g*). Concentrated cell suspensions (~10^3 cells nl^{-1}) were front loaded into beveled glass micropipettes (~50-μm tip diameter, Wiretol 5 μl, Drummond Scientific) and bilaterally injected (5×10^4 cells per injection) into dorsal hippocampus of WT or $Chd2^{+/-}$ littermates at P5 as described previously (Hunt et al., 2013; Vogt et al., 2014).

Quantification and Statistical Analysis

Samples were randomly collected across litters and processed blind to genotype. All analyses were performed with SYSTAT 13.1 software and assessed for normality (Shapiro-Wilk) and variance (Brown-Forsythe). Mossy fiber sprouting scores and intrinsic electrophysiological properties were assessed by nonparametric Mann-Whitney U test on ranks. All other data were compared by two-tailed t-test, one-way ANOVA for multiple comparisons or by two-way repeated measures ANOVA. A Tukey's *post hoc* test was performed when appropriate. Sample sizes for behavior assays were determined by power

analyses using 20% as a value for β (1 – β = power or 80%), 0.05 as a value for α and an expected 30% difference between groups; post-hoc power for each behavior assay is indicated in Table S7. No statistical methods were used to predetermine sample size in other experiments. Sample sizes can be found within results and/or figure legends, and individual data points are shown for each quantification. For slice electrophysiology studies, experimental data were averaged across neurons (i.e., *n* = neurons). In all other studies, experimental data were averaged across animals (i.e., n = mice). Data are expressed as mean ± standard error (s.e.m.) and significance was set at P<0.05. For differential gene expression analysis, significance was set at FDR < 0.10 and $P < 0.05$.

KEYRESOURCES TABLE

The table highlights the genetically modified organisms and strains, cell lines, reagents, software, and source data **essential** to reproduce results presented in the manuscript. Depending on the nature of the study, this may include standard laboratory materials (i.e., food chow for metabolism studies), but the Table is **not** meant to be comprehensive list of all materials and resources used (e.g.,essential chemicals such as SDS, sucrose, or standard culture media don't need to be listed in the Table). **Items in the Table must also be reported in the Method Details section within the context of their use.**The number of **primers and RNA sequences** that may be listed in the Tableis restricted to no more than ten each. If there are more than ten primers or RNA sequences to report, please provide this information as a supplementary document and reference this file (e.g., See Table S1 for XX) in the Key Resources Table.

Please note that ALL references cited in the Key Resources Table must be included in the References list. Please report the information as follows:

- **REAGENT or RESOURCE:** Provide full descriptive name of the item so that it can be identified and linked with its description in the manuscript (e.g., provide version number for software, host source for antibody, strain name). In the Experimental Models section, please include all models used in the paper and describe each line/strain as: model organism: name used for strain/line in paper: genotype. (i.e.,Mouse: $OXTR^{fl/fl}$: B6.129(SJL)-$Oxtr^{tm1.1Wsy/J}$). In the Biological Samples section, please list all samples obtained from commercial sources or biological repositories. Please note that software mentioned in the Methods Details or Data and Software Availability section needs to be also included in the table.See the sample Table at the end of this document for examples of how to report reagents.
- **SOURCE:** Report the company, manufacturer, or individual that provided the item or where the item can obtained (e.g., stock center or repository). For materials distributed by Addgene, please cite the article describing the plasmid and include "Addgene" as part of the identifier. If an item is from another lab, please include the name of the principal investigator and a citation if it has been previously published. If the material is being reported for the first time in the current paper, please indicate as "this paper." For software, please provide the

company name if it is commercially available or cite the paper in which it has been initially described.

- **IDENTIFIER:** Include catalog numbers (entered in the column as “Cat#” followed by the number, e.g., Cat#3879S).Where available, please include unique entities such as RRIDs, Model Organism Database numbers, accession numbers, and PDB or CAS IDs. For antibodies, if applicable and available, please also include the lot number or clone identity. For software or data resources, please include the URL where the resource can be downloaded. Please ensure accuracy of the identifiers,as they are essential for generation ofhyperlinks toexternal sources when available. Please see the Elsevierlist of Data Repositorieswith automated bidirectional linking for details. Whenlisting more than one identifier for the same item, use semicolons to separate them (e.g. Cat#3879S; RRID: AB_2255011). If an identifier is not available, please enter “N/A” in the column.
  - ***A NOTE ABOUT RRIDs:*** We highly recommend using RRIDs as the identifier (in particular for antibodies and organisms, but also for software tools and databases). For more details on how to obtain or generate an RRID for existing or newly generated resources, please visit the RII or search for RRIDs.

Please use the empty table that follows to organize the information in the sections defined by the subheading, skipping sections not relevant to your study. Please do not add subheadings.To add a row, place the cursorat the end of the row above where you would like to add the row, just outside the right border of the table. Then press the ENTER key to add the row. Please delete empty rows. Each entry must be on a separate row; do not list multiple items in a single table cell. Please see the sample table at the end of this document for examples of how reagents should be cited.

Supplementary Material

Refer to Web version on PubMed Central for supplementary material.

Acknowledgements

This work was supported by funding from the Lennox-Gastaut Syndrome Foundation, National Institutes of Health grants NINDS R00–NS085046, R01–NS096012 and T32–NS045540, UCI SURP and UROP Fellowship Programs, UCI Center for Autism Research and Translation (CART) and UCLA QCBio Collaboratory. We thank Haico van Attikum, Martijn Luijsterburg and Wouter Wiegant for generously sharing western blot protocols; Daniel Vogt and John Rubenstein for kindly sharing GAD67-GFP mice; Sarah Smith and Kimberly Gonzalez for genotyping; Alex Lee with assistance with genotyping and immunostaining; Jenny Wu and the UCI Genomics High-Throughput Facility for sequence alignment of RNA sequencing; and Daniel Vogt, Kei Igarashi and Scott Baraban for helpful discussions and comments on earlier versions of this manuscript.

References

Atallah BV, Scanziani M (2009) Instaneous modulation of gamma oscillation frequency by balancing excitation with inhibition. Neuron 62, 566–577. [PubMed: 19477157]

Buckmaster PS (2012) Mossy fiber sprouting in the dentate gyrus. Jasper's Basic Mechanisms of the Epilepsies 4th edn Eds: Noebels JL, Avoli M, Rogawski MA, Olsen RW, Delgado-Escueta AV (National Center for Biotechnology, Bethesda Maryland).

Cain-Hom C, Splinter E, Min MV, Simonis M, van de Heigning M, Martinez M, Asghari V, Cox JC, Warmin S (2017) Efficient mapping of transgene integration sites and local structural changes in Cre transgenic mice using targeted locus amplification. Nuc Acid Res 45, e62.

Carlén M, Meletis K, Siegle JH, Cardin JA, Futai K, Vierling-Claassen D, Rühlmann C, Jones SR, Deisseroth K, Sheng M, Moore CI, Tsai LH (2012) A critical role for NMDA receptors in parvalbumin interneurons for gamma rhythm induction and behavior. Mol. Psychiatry 17, 537–548. [PubMed: 21468034]

Carvill GL, Heavin SB, Yendle SC, McMahon JM, O'Roak BJ, Cook J, Khan A, Dorschner MO, Weaver M, Calvert S, Malone S, Wallace G, Stanley T, Bye AM, Bleasel A, Howell KB, Kivity S, Mackay MT, Rodriguez-Casero V, Webster R, Korczyn A, Afawi Z, Zelnick N, Lerman-Sagie T, Lev D, Møller RS, Gill D, Andrade DM, Freeman JL, S adleir LG, Shendure J, Berkovic SF, Scheffer IE, Mefford H (2013) Targeted resequencing in epileptic encephalopathies identifies de novo mutations in CHD2 and SYNGAP1. Nat Genet 45, 825–830. [PubMed: 23708187]

Carvill G, Helbig I, Mefford H (2015) CHD2-related neurodevelopmental disorders. In: Pagon RA, Adam MP, Ardinger HH, Wallace SE, Amemiya A, Bean LJH, Bird TD, Ledbetter N, Mefford HC, Smith RJH, Stephens K, editors. GeneReviews® [Internet] Seattle (WA): University of Washington, Seattle.

Chénier S, Yoon G, Argiropoulos B, Lauzon J, Laframboise R, Ahn JW, Ogilvie CM, Lionel AC, Marshall CR, Vaags AK, Hashemi B, Boisvert K, Mathonnet G, Tihy F, So J, Scherer SW, Lemyre E, Stavropoulos DJ (2014) CHD2 haploinsufficiency is associated with developmental delay, intellectual disability, epilepsy and neurobehavioural problems. J Neurodev Disord 6, 9. [PubMed: 24834135]

Cho KK, Hoch R, Lee AT, Patel T, Rubenstein JL, Sohal VS (2015) Gamma rhythms link prefrontal interneuron dysfunction with cognitive inflexibility in Dlx5/6(+/−) mice. Neuron 85, 1332–43. [PubMed: 25754826]

Cornew L, Roberts TP, Blaskey L, Edgar JC. Resting-state oscillatory activity in autism spectrum disorders (2013) J Autism Dev Disord 42, 1884–94.

Deciphering Developmental Disorders Study (2015) Large-scale discovery of novel genetic causes of developmental disorders. Nature 519, 223–8. [PubMed: 25533962]

de Lanerolle NC, Kim JH, Robbins RJ, Spencer DD (1989) Hippocampal interneuron loss and plasticity in human temporal lobe epilepsy. Brain Res 495:387–395. [PubMed: 2569920]

Del Pino I, García-Frigola C, Dehorter N, Brotons-Mas JR, Alvarez-Salvado E, Martínez de Lagrán M, Ciceri G, Gabaldón MV, Moratal D, Dierssen M, Canals S, Marín O, Rico B (2013) Erbb4 deletion from fast-spiking interneurons causes schizophrenia-like phenotypes. Neuron 79, 1152–1168. [PubMed: 24050403]

De Rubeis S, He X, Goldberg AP, Poultney CS, Samocha K, Cicek AE, Kou Y, Liu L, Fromer M, Walker S, Singh T, Klei L, Kosmicki J, Shih-Chen F, Aleksic B, Biscaldi M, Bolton PF, Brownfeld JM, Cai J, Campbell NG, Carracedo A, Chahrour MH, Chiocchetti AG, Coon H, Crawford EL, Curran SR, Dawson G, Duketis E, Fernandez BA, Gallagher L, Geller E, Guter SJ, Hill RS, Ionita-Laza J, Jimenz Gonzalez P, Kilpinen H, Klauck SM, Kolevzon A, Lee I, Lei I, Lei J, Lehtimäki T, Lin CF, Ma'ayan A, Marshall CR, McInnes AL, Neale B, Owen MJ, Ozaki N, Parellada M, Parr JR, Purcell S, Puura K, Rajagopalan D, Rehnström K, Reichenberg A, Sabo A, Sachse M, Sanders SJ, Schafer C, Schulte-Rüther M, Skuse D, Stevens C, Szatmari P, Tammimies K, Valladares O, Voran A, Li-San W, Weiss LA, Willsey AJ, Yu TW, Yuen RK; Study DDD; Homozygosity Mapping Collaborative for Autism; UK10K Consortium, Cook EH, Freitag CM, Gill M, Hultman CM, Lehner T, Palotie A, Schellenberg GD, Sklar P, State MW, Sutcliffe JS, Walsh CA, Scherer SW, Zwick ME, Barett JC, Cutler DJ, Roeder K, Devlin B, Daly MJ, Buxbaum JD (2014) Synaptic, transcriptional and chromatin genes disrupted in autism. Nature 515, 209–15. [PubMed: 25363760]

Durak O, Gao F, Kaeser-Woo YJ, Rueda R, Martorell AJ, Nott A, Liu CY, Watson LA, Tsai LH (2016) Chd8 mediates cortical neurogenesis via transcriptional regulation of cell cycle and Wnt signaling. Nat Neurosci 19,1477–1488. [PubMed: 27694995]

Epi4K Consortium; Epilepsy Phenome/Genome Project, Allen AS, Berkovic SF, Cossette P, Delanty N, Dlugos D, Eichler EE, Epstein MP, Glauser T, Goldstein DB, Han Y, Heinzen EL, Hitomi Y, Howell KB, Johnson MR, Kuzniecky R, Lowenstein DH, Lu YF, Madou MR, Marson AG, Mefford HC, Esmaeeli Nieh S, O'Brien TJ, Ottman R, Petrovski S, Poduri A, Ruzzo EK, Scheffer IE, Sherr EH, Yuskaitis CJ, Abou-Khalil B, Alldredge BK, Bautista JF, Berkovic SF, Boro A, Cascino GD, Consalvo D, Crumrine P, Devinsky O, Dlugos D, Epstein MP, Fiol M, Fountain NB, French J, Friedman D, Geller EB, Glauser T, Glynn S, Haut SR, Hayward J, Galizia EC, Myers CT, Leu C, de Kovel CG, Afrikanova T, Cordero-Maldonado ML, Martins TG, Jacmin M, Drury S, Krishna Chinthapalli V, Muhle H, Pendziwiat M, Sander T, Ruppert AK, Møller RS, Thiele H, Krause R, Schubert J, Lehesjoki AE, Nürnberg P, Lerche H; EuroEPINOMICS CoGIE Consortium, Palotie A, Coppola A, Striano S, Gaudio LD, Boustred C, Schneider AL, Lench N, Jocic-Jakubi B, Covanis A, Capovilla G, Veggiotti P, Piccioli M, Parisi P, Cantonetti L, Sadleir LG, Mullen SA, Berkovic SF, Stephani U, Helbig I, Crawford AD, Esguerra CV, Kasteleijn-Nolst Trenité DG, Koeleman BP, Mefford HC, Scheffer IE, Sisodiya SM (2015) CHD2 variants are a risk factor for photosensitivity in epilepsy. Brain 138, 1198–207. [PubMed: 25783594]

Gompers AL, Su-Feher L, Ellegood J, Copping NA, Riyadh MA, Stradleigh TW, Pride MC, Schaffler MD, Wade AA, Catta-Preta R, Zdilar I, Louis S, Kaushik G, Mannion BJ, Plajzer-Frick I, Afzal V, Visel A, Pennacchio LA, Dickel DE, Lerch JP, Crawley JN, Zarbalis KS, Silverman JL, Nord AS (2017) Germline Chd8 haploinsufficiency alters brain development in mouse. Nat Neurosci 20, 1062–1073. [PubMed: 28671691]

Hamdan FF, Srour M, Capo-Chichi JM, Daud H, Nassif C, Patry L, Massicotte C, Ambalavanan A, Spiegelman D, Diallo O, Henrion E, Dionne-Laporte A, Fougerat A, Pshezhetsky AV, Venkateswaran S, Rouleau GA, Michaud JL (2014) De novo mutations in moderate or severe intellectual disability. PLoS Genet 10, e1004772. [PubMed: 25356899]

Harada A, Okada S, Konno D, Odawara J, Yoshimi T, Yoshimura S, Kumamaru H, Saiwai H, Tsubota T, Kurumizaka H, Akashi K, Tachibana T, Imbalzano AN, Ohkawa Y (2012) Chd2 interacts with H3.3 to determine myogenic cell fate. EMBO J 31, 2994–3007. [PubMed: 22569126]

Helmers SL, Joshi S, Kanner A, Kirsch HE, Knowlton RC, Kossoff EH, Kuperman R, Kuzniecky R, Lowenstein DH, McGuire SM, Motika PV, Novotny EJ, Ottman R, Paolicchi JM, Parent JM, Park K, Poduri A, Scheffer IE, Shellhaas RA, Sherr EH, Shih JJ, Singh R, Sirven J, Smith MC, Sullivan J, Lin Thio L, Venkat A, Vining EP, Von Allmen GK, Weisenberg JL, Widdess-Walsh P, Winawer MR (2013) De novo mutations in epileptic encephalopathies. Nature 12, 501, 217–21.

Hirsch JC, Agassandian C, Merchán-Pérez A, Ben-Ari Y, DeFelipe J, Esclapez M, Bernard C (1999) Deficit of quantal release of GABA in experimental models of temporal lobe epilepsy. Nat Neurosci 2, 499–500. [PubMed: 10448211]

Howard MA, Rubenstein JL, Baraban SC (2013) Bidirectional homeostatic plasticity induced by interneuron cell death and transplantation in vivo. Proc Natl Acad Sci USA 111, 492–7. [PubMed: 24344303]

Hunt RF, Girskis KM, Rubenstein JL, Alvarez-Buylla A, Baraban SC (2013) GABA progenitors grafted into the adult epileptic brain control seizures and abnormal behavior. Nat Neurosci 16, 692–697. [PubMed: 23644485]

Hunt RF, Scheff SW, Smith BN (2009) Posttraumatic epilepsy after controlled cortical impact injury in mice. Exp Neurol 215, 243–252. [PubMed: 19013458]

Iossifov I, O'Roak BJ, Sanders SJ, Ronemus M, Krumm N, Levy D, Stessman HA, Witherspoon KT, Vives L, Patterson KE, Smith JD, Paeper B, Nickerson DA, Dea J, Dong S, Gonzalez LE, Mandell JD, Mane SM, Murtha MT, Sullivan CA, Walker MF, Waqar Z, Wei L, Willsey AJ, Yamrom B, Lee YH, Grabowska E, Dalkic E, Wang Z, Marks S, Andrews P, Leotta A, Kendall J, Hakker I, Rosenbaum J, Ma B, Rodgers L, Troge J, Narzisi G, Yoon S, Schatz MC, Ye K, McCombie WR, Shendure J, Eichler EE, State MW, Wigler M (2014) The contribution of de novo coding mutations to autism spectrum disorder. Nature 515, 216–21. [PubMed: 25363768]

Jensen EC (2013) Quantitative analysis of histological staining and fluorescence using ImageJ. Anat Rec 296, 378–81.

Katayama Y, Nishiyama M, Shoji H, Ohkawa Y, Kawamura A, Sato T, Suyama M, Takumi T, Miyakawa T, Nakayama KI (2016) CHD8 haploinsufficiency results in autistic-like phenotypes in mice. Nature 537, 675–679. [PubMed: 27602517]

Khoshkhoo S, Vogt D, Sohal V (2017) Dynamic, Cell-Type-Specific Roles for GABAergic Interneurons in a Mouse Model of Optogenetically Inducible Seizures. Neuron 2, 291–298.

Korotkova T, Fuchs EC, Ponomarenko A, von Engelhardt J, Monyer H (2010) NMDA receptor ablation on parvalbumin-positive interneurons impairs hippocampal synchrony, spatial representations, and working memory. Neuron 68, 557–569. [PubMed: 21040854]

Kulkarni S, Nagarajan P, Wall J, Donovan DJ, Donell RL, Ligon AH, Venkatachalam S, Quade BJ (2008) Disruption of chromodomain helicase DNA binding protein 2 (CHD2) causes scoliosis. Am J Med Genet A 146A, 1117–27. [PubMed: 18386809]

Kwan V, Unda BK, Singh KK (2016) Wnt signaling networks in autism spectrum disorder and intellectual disability. J Neurodev Dis 8, 45.

Levenson JM, Sweatt JD (2013) Epigenetic mechanisms in memory formation. Nat Rev Neurosci 6, 108–118.

Lim S, Goldman MS (2013) Balanced cortical microcircuitry for maintaining information in working memory. Nat Neurosci 16, 1306–1314. [PubMed: 23955560]

Love MI, Huber W, Anders S (2014) Moderated estimation of fold change and dispersion for RNA-seq data with DESeq2. Genome Biol 15, 550. [PubMed: 25516281]

Luijsterburg MS, de Krijger I, Wiegant WW, Shah RG, Smeenk G, de Groot AJ, Pines A, Vertegaal AC, Jacobs JJ, Shah GM, van Attikum H (2016) PARP1 Links CHD2-Mediated Chromatin Expansion and H3.3 Deposition to DNA Repair by Non-homologous End-Joining. Mol Cell 18, 547–562.

Marfella CG, Henninger N, LeBlanc SE, Krishnan N, Garlick DS, Holzman LB, Imbalzano AN (2008) A mutation in the mouse Chd2 chromatin remodeling enzyme results in a complex renal phenotype. Kidney Blood Press Res 31(6): 421–32. [PubMed: 19142019]

Marfella CG, Imbalzano AN (2007) The Chd2 family of chromatin remodelers. Mutat Res 618, 30–40. [PubMed: 17350655]

Marfella CG, Ohkawa Y, Coles AH, Garlick DS, Jones SN, Imbalzano AN (2006) Mutation of the SNF2 family member Chd2 affects mouse development and survival. J Cell Physiol 209,162–171. [PubMed: 16810678]

Mastrototaro G, Zaghi M, Sessa A (2017) Epigenetic mistakes in neurodevelopmental disorders. J Molec Neurosci 61, 590–602. [PubMed: 28255957]

Meganathan K, Lewis EMA, Gontarz P, Liu S, Stanley EG, Elefanty AG, Huettner JE, Zhang B, Kroll KL (2017) Regulatory networks specifying cortical interneurons from human embryonic stem cells reveal roles for CHD2 in interneuron development. Proc Natl Acad Sci 114, E11180–E11189. [PubMed: 29229852]

Mews P, Donahue G, Drake AM, Luczak V, Abel T, Berger SL (2017) Acetyl-CoA synthetase regulates histone acetylation and hippocampal memory. Nature 546, 381–386. [PubMed: 28562591]

Neale BM, Kou Y, Liu L, Ma'ayan A, Samocha KE, Sabo A, Lin CF, Stevens C, Wang LS, Makarov V, Polak P, Yoon S, Maguire J, Crawford EL, Campbell NG, Geller ET, Valladares O, Schafer C, Liu H, Zhao T, Cai G, Lihm J, Dannenfelser R, Jabado O, Peralta Z, Nagaswamy U, Muzny D, Reid JG, Newsham I, Wu Y, Lewis L, Han Y, Voight BF, Lim E, Rossin E, Kirby A, Flannick J, Fromer M, Shakir K, Fennell T, Garimella K, Banks E, Poplin R, Gabriel S, DePristo M, Wimbish JR, Boone BE, Levy SE, Betancur C, Sunyaev S, Boerwinkle E, Buxbaum JD, Cook EH Jr, Devlin B, Gibbs RA, Roeder K, Schellenberg GD, Sutcliffe JS, Daly MJ (2012) Patterns and rates of exonic de novo mutations in autism spectrum disorders. Nature 485, 242–5. [PubMed: 22495311]

Newman JC, Covarrubias AJ, Zhao M, Yu X, Gut P, Ng CP, Huang Y, Haldar S, Verdin E (2017) Ketogenic Diet Reduces Midlife Mortality and Improves Memory in Aging Mice. Cell Metab 26, 547–557. [PubMed: 28877458]

Opperman KJ, Mulcahy B, Giles AC, Risley MG, Birnbaum RL, Tulgren ED, Dawson-Scully K, Zhen M6, Grill B (2017) The HECT Family Ubiquitin Ligase EEL-1 Regulates Neuronal Function and Development. Cell Rep 19:822–835. [PubMed: 28445732]

Orekhova EV, Stroganova TA, Nygren G, Tsetlin MM, Posikera IN, Gillberg C, Elam M (2007) Excess of high frequency electroencephalogram oscillations in boys with autism. Biol Psychiatry 62, 1022–9. [PubMed: 17543897]

O'Roak BJ, Stessman HA, Boyle EA, Witherspoon KT, Martin B, Lee C, Vives L, Baker C, Hiatt JB, Nickerson DA, Bernier R, Shendure J, Eichler EE (2014) Recurrent de novo mutations implicate novel genes underlying simplex autism risk. Nat Commun 24, 5595.

Platt RJ, Zhou Y, Slaymaker IM, Shetty AS, Weisbach NR, Kim JA, Sharma J, Desai M, Sood S, Kempton HR, Crabtree GR, Feng G, Zhang F (2017) Chd8 mutation leads to autistic-like behaviors and impaired striatal circuits. Cell Rep 19, 335–350. [PubMed: 28402856]

Petryniak MA, Potter GB, Rowitch DH, Rubenstein JL (2007) Dlx1 and Dlx2 control neuronal versus oligodendroglial cell fate acquisition in the developing forebrain. Neuron 2, 417–33.

Rauch A, Wieczorek D, Graf E, Wieland T, Endele S, Schwarzmayr T, Albrecht B, Bartholdi D, Beygo J, Di Donato N, Dufke A, Cremer K, Hempel M, Horn D, Hoyer J, Joset P, Röpke A, Moog U, Riess A, Thiel CT, Tzschach A, Wiesener A, Wohlleber E, Zweier C, Ekici AB, Zink AM, Rump A, Meisinger C, Grallert H, Sticht H, Schenck A, Engels H, Rappold G, Schröck E, Wieacker P, Riess O, Meitinger T, Reis A, Strom TM (2012) Range of genetic mutations associated with severe non-syndromic sporadic intellectual disability: an exome sequencing study. Lancet 380, 1674–82. [PubMed: 23020937]

Satoh J, Tabira T, Sano M, Nakayama H, Tateishi J (1991) Parvalbumin-immunoreactive neurons in the human central nervous system are decreased in Alzheimer's disease. Acta Neuropathologica 81:388–395. [PubMed: 2028743]

Sharfman HE (2015) Metabolic control of epilepsy. Science 347, 1312–1313. [PubMed: 25792315]

Shen T, Ji F, Yuan Z, Jiao J (2015) CHD2 is required for embryonic neurogenesis in the developing cerebral cortex. Stem Cells 33, 1794–806. [PubMed: 25786798]

Southwell DG, Paredes MF, Galvao RP, Jones DL, Froemke RC, Sebe JY, Alfaro-Cervello C, Tang Y, Garcia-Verdugo JM, Rubenstein JL, Baraban SC, Alvarez-Buylla A (2012) Intrinsically determined cell death of developing cortical interneurons. Nature 1, 109–13.

Sokpor G, Xie Y, Rosenbusch J, Tuoc T (2017) Chromatin Remodeling BAF (SWI/SNF) Complexes in Neural Development and Disorders. Front Mol Neurosci 10, 243. [PubMed: 28824374]

Tamamaki Yanagawa Y, Tomioka R, Miyazaki J, Obata K, Kaneko T (2003) Green fluorescent protein expression and colocalization with calretinin, parvalbumin, and somatostatin in the GAD67–GFP knock-in mouse. J. Comp. Neurol 467, 60–79. [PubMed: 14574680]

Tauck DL, Nadler JV (1985) Evidence of functional mossy fiber sprouting in hippocampal formation of kainic acid-treated rats. J Neurosci 5, 1016–1022. [PubMed: 3981241]

Tyagi M, Imam N, Verma K, Patel AK (2016) Chromatin remodelers: We are the drivers!! Nucleus 3, 388–404.

Vaudano AE, Ruggieri A, Avanzini P, Gessaroli G, Cantalupo G, Coppola A, Sisodiya SM, Meletti S (2017) Photosensitive epilepsy is associated with reduced inhibition of alpha rhthm generating networks. Brain 140, 981–997. [PubMed: 28334965]

Vogel-Ciernia A, Matheos DP, Barrett RM, Kramár EA, Azzawi S, Chen Y, Magnan CN, Zeller M, Sylvain A, Haettig J, Jia Y, Tran A, Dang R, Post RJ, Chabrier M, Babayan AH, Wu JI, Crabtree GR, Baldi P, Baram TZ, Lynch G, Wood MA (2013a) The neuron-specific chromatin regulatory subunit BAF53b is necessary for synaptic plasticity and memory. Nat Neurosci 16, 552–61. [PubMed: 23525042]

Vogel-Ciernia A, Wood MA (2013b) Examining object location and object recognition memory in mice. Curr Protoc Neurosci 69, 1–17.

Vogt D, Hunt RF, Mandal S, Sandberg M, Silberberg SN, Nagasawa T, Yang Z, Baraban SC, Rubenstein JLR. (2014) Lhx6 directly regulates Arx and CXCR7 to determine cortical interneuron fate and laminar position. Neuron 82(2):350–364. [PubMed: 24742460]

Willoughby JO, Fitzgibbon SP, Pope KJ, Mackenzie L, Medvedev AV, Clark CR, Davey MP, Wilcox RA (2003) Persistent abnormality detected in the non-ictal electroencephalogram in primary generalised epilepsy. J Neurol Neurosurg Psychiatry 74, 51–55. [PubMed: 12486266]

Young MD, Wakefield MJ, Smyth GK, Oshlack A (2010) Gene ontology analysis for RNA-seq: accounting for selection bias. Genome Biol 11, R14. [PubMed: 20132535]

Yu G, Wang L-G, Yan G-R, He Q-Y (2015) DOSE: an R/Bioconductor package for disease ontology semantic and enrichment analysis. Bioinformatics 31, 608–609. [PubMed: 25677125]

Highlights

- CHD2 is widely expressed in the embryonic and mature brain
- *G*ene expression is broadly altered by *Chd2*$^{+/-}$
- *Chd2*$^{+/-}$ mice have deficits in neuron proliferation, synaptic function and memory
- Interneuron transplantation rescues memory problems in *Chd2*$^{+/-}$ mice

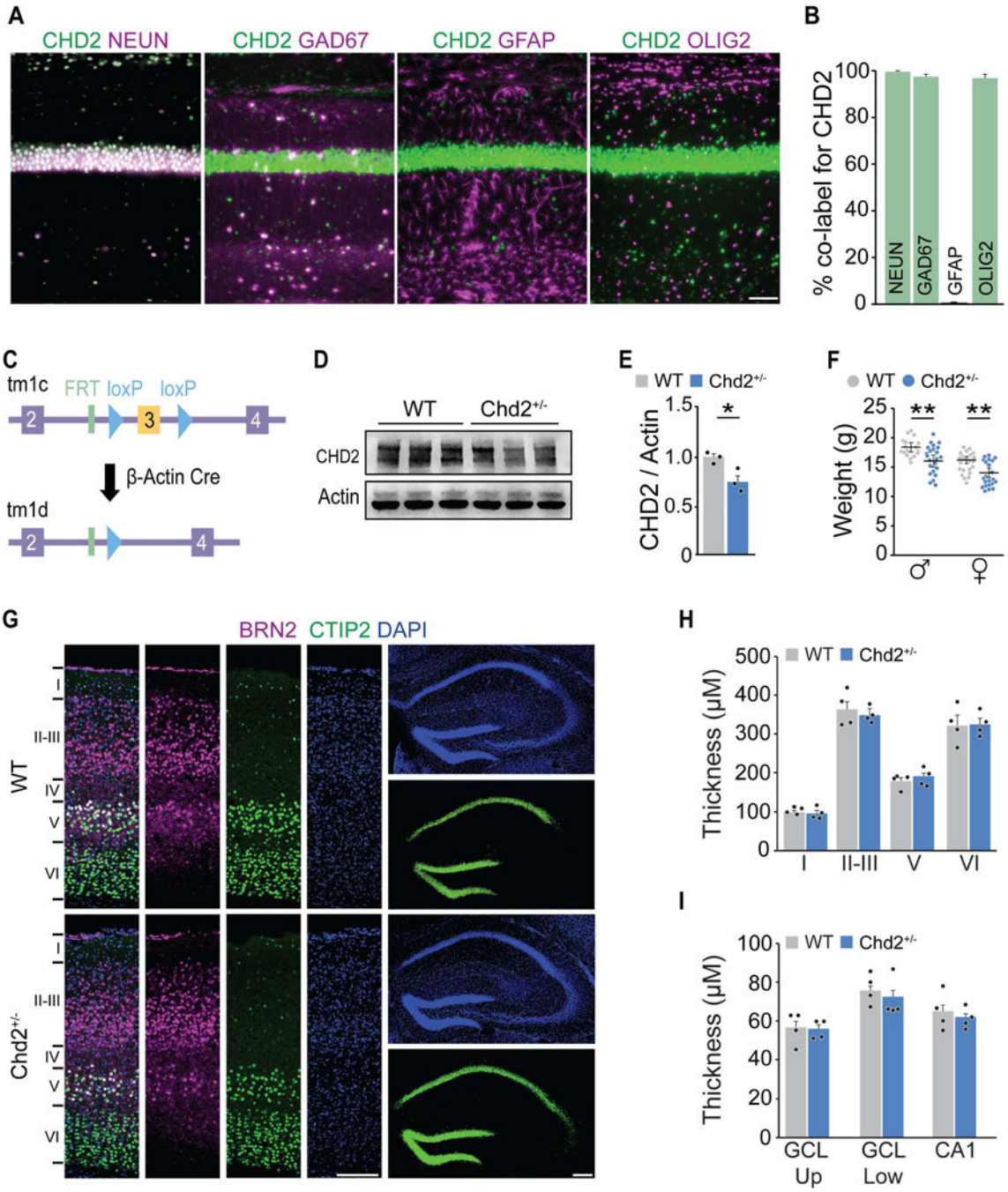

Figure 1. Generation of *Chd2*$^{+/-}$ mice.

A. At P30, CHD2 (green) co-labeled with NEUN, GAD67 and OLIG2, but not GFAP (all in magenta). **B.** Quantification of CHD2 expression in each cell type (n=3 mice per marker). **C.** Schematic of the conditional allele for Chd2 (tm1c). Cre deletes the floxed exon 3 of Chd2 to generate a frame shift mutation (tm1d). **D, E.** Western blot analysis for CHD2 and Actin showed reduction of CHD2 protein in Chd2+/− brain at P30 (P= 0.027, n=3 mice per genotype). **F.** Mean body weight of male and female Chd2+/− mice was reduced compared to WT littermates (n=17–23 mice per genotype). **G.** Immunostaining for BRN2 (magenta),

CTIP2 (green) and DAPI in somatosensory cortex (left panels) and hippocampus (right panels) at P30. **H.** Thickness of individual cell layers in somatosensory cortex (SS Ctx) was not altered by Chd2+/− (n = 4 mice per genotype). **I.** Width of granule cell layer (GCL) or CA1 pyramidal cell layer (CA1) was not altered by Chd2+/− (n = 4 mice per genotype). Error bars, s.e.m.; ∗ $p < 0.05$. ∗∗ $p < 0.01$; scale bars, 75 μm in A and 150 μm in G. See also Figure S1.

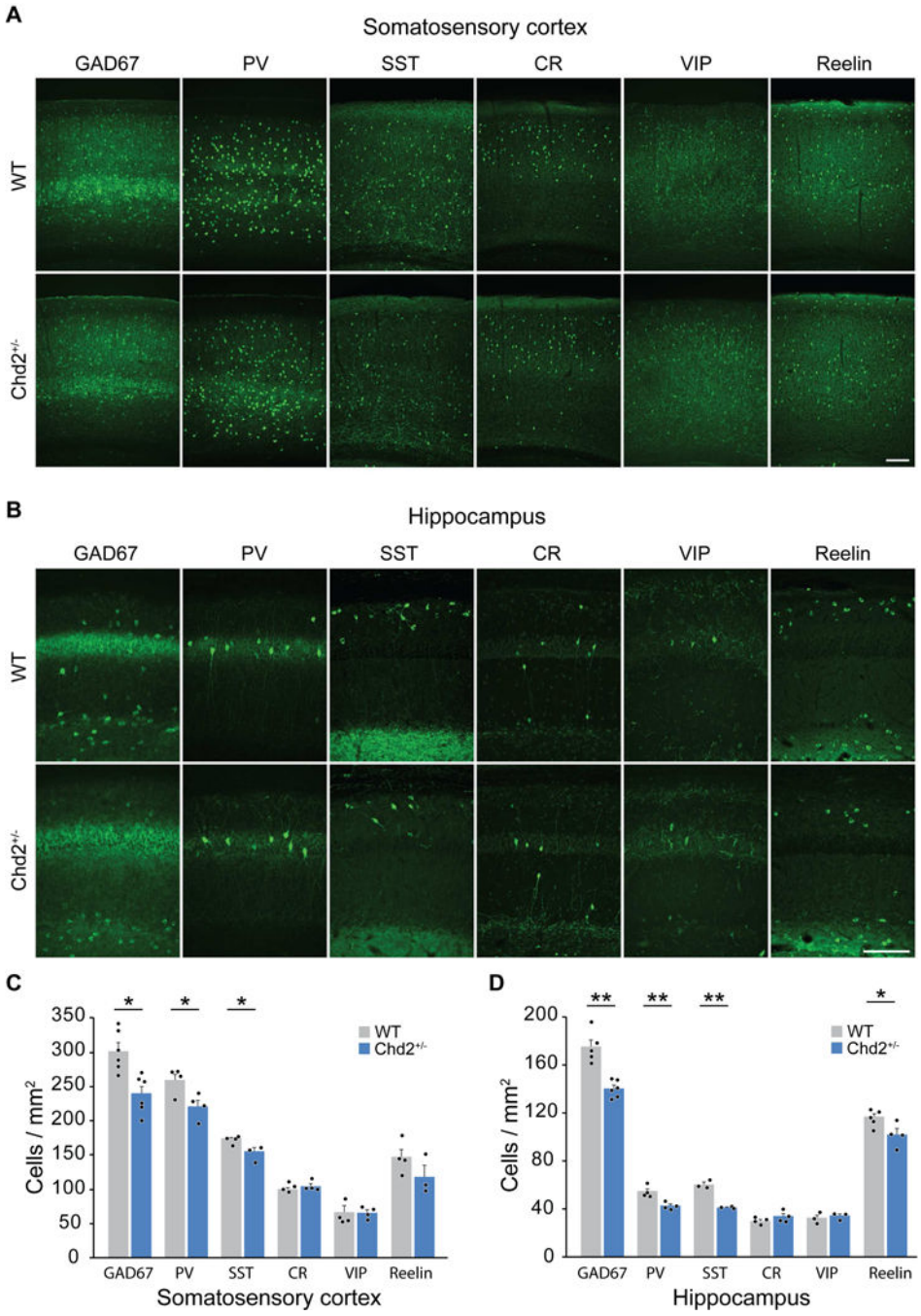

Figure 2. *Chd2*$^{+/-}$ mice exhibit decreased density of GABAergic interneurons.

A, B. Immunostaining of coronal sections through somatosensory neocortex (**A**) and CA1 region of hippocampus (**B**) for GAD67, PV, SST, CR, VIP and reelin at P30. **C, D.** Quantification of each subtype marker shows Chd2+/− mice had decreased density of cells expressing GAD67, PV and SST in somatosensory cortex (**C**) and decreased density of cells expressing GAD67 PV, SST and reeling in hippocampus (**D**) compared to WT littermates (n=3–6 mice per genotype). Error bars, s.e.m.; ∗ $p < 0.05$. ∗∗ $p < 0.01$; scale bars, 150 μm in A and B. See also Figure S2 and S3.

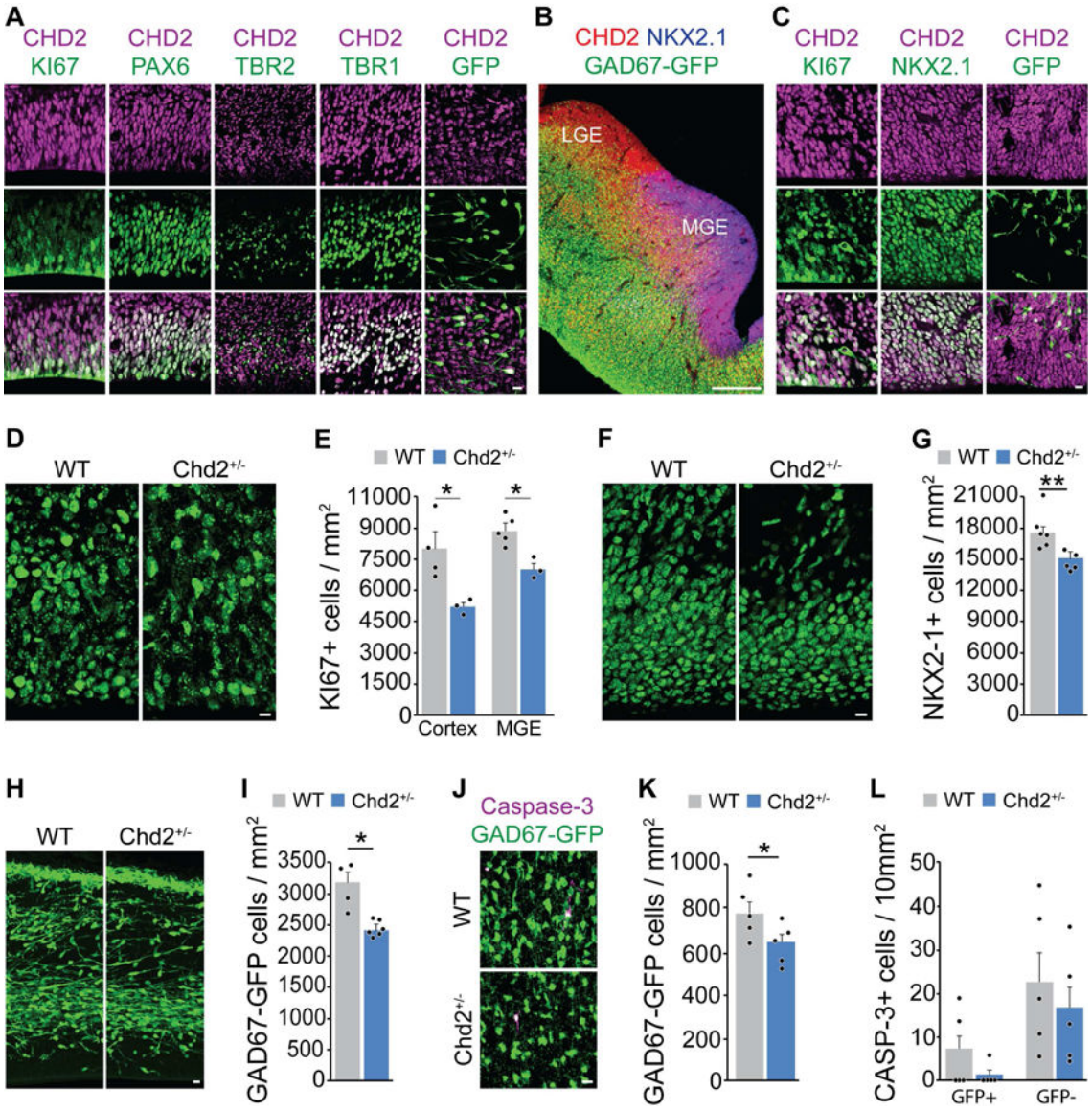

Figure 3. Chd2 regulates proliferation of neural progenitors in developing forebrain.

A. Immunostaining for CHD2 (magenta) and Ki67, Pax6, Tbr2, Tbr1 and GAD67-GFP (all green) in neocortex at E14.5. **B.** Immunostaining for CHD2 (red), Nkx2.1 (blue) and GAD67-GFP (green) in ventral telencephalon shows CHD2 expression in GABAergic progenitor domains at E14.5. **C.** At E14.5, CHD2 (magenta) co-labeled with Ki67 and Nkx2.1, but not GAD67-GFP (all in green) in MGE. Lower magnification images of dorsal and ventral telencephalon are shown in Figure S4. **D, E.** At E14.5, the density of Ki67+ cells were reduced in MGE and cortex of Chd2+/− mice (n=3–5 mice per genotype). **F, G.** At E14.5, the density of Nkx2.1+ GABA progenitors were reduced in MGE of Chd2+/− mice (n=5–6 mice per genotype). H, I. At E14.5, the density of GAD67-GFP progenitors were reduced in cortex of Chd2+/− mice (n=4–6 mice per genotype). **J-L.** At P7, immunostaining analysis revealed a reduction in GAD67-GFP progenitors in somatosensory neocortex, but the density of cells expressing caspase-3 (CASP3) was not different between genotypes (n=5

mice per genotype). Error bars, s.e.m.; ∗ $p < 0.05$; ∗∗ $p < 0.01$; scale bars, 10 μm in A and C, 200 μm in B, and 20 μm in **D, F, H, J.** See also Figure S4.

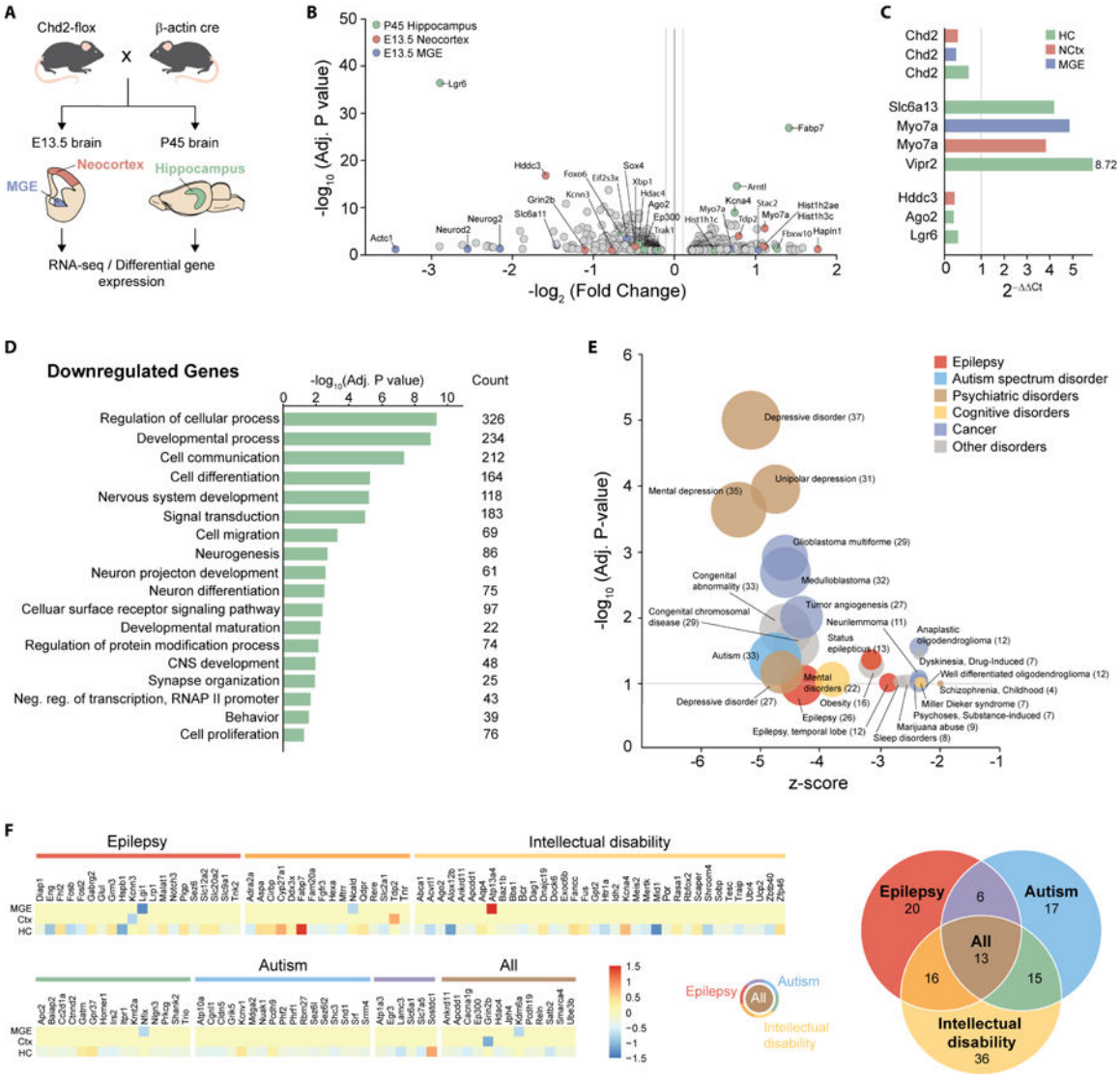

Figure 4. *Chd2* haploinsufficiency disrupts genes necessary for early cortical development and synaptic function.

A. Schematic showing the experimental approach used for RNA-sequencing. **B.** Volcano plot displaying genes that were significantly differentially expressed (Adj. P < 0.1) in Chd2+/− mice (n=3 mice per genotype). **C.** qRT-PCR validation of DE genes predicted by RNA-sequencing. **D.** Gene ontology for down-regulated genes at P45. Complete gene ontology is provided in Table S3. **E.** Plot of z-score by -log10 of the adjusted P-value for human diseases identified by disease ontology. The complete disease ontology is provided in Table S5. **F.** Heatmaps of genes associated with childhood epilepsy, intellectual disability and autism spectrum disorder that were differentially expressed in E13.5 MGE, E13.5 Neocortex and/or P45 Hippocampus.

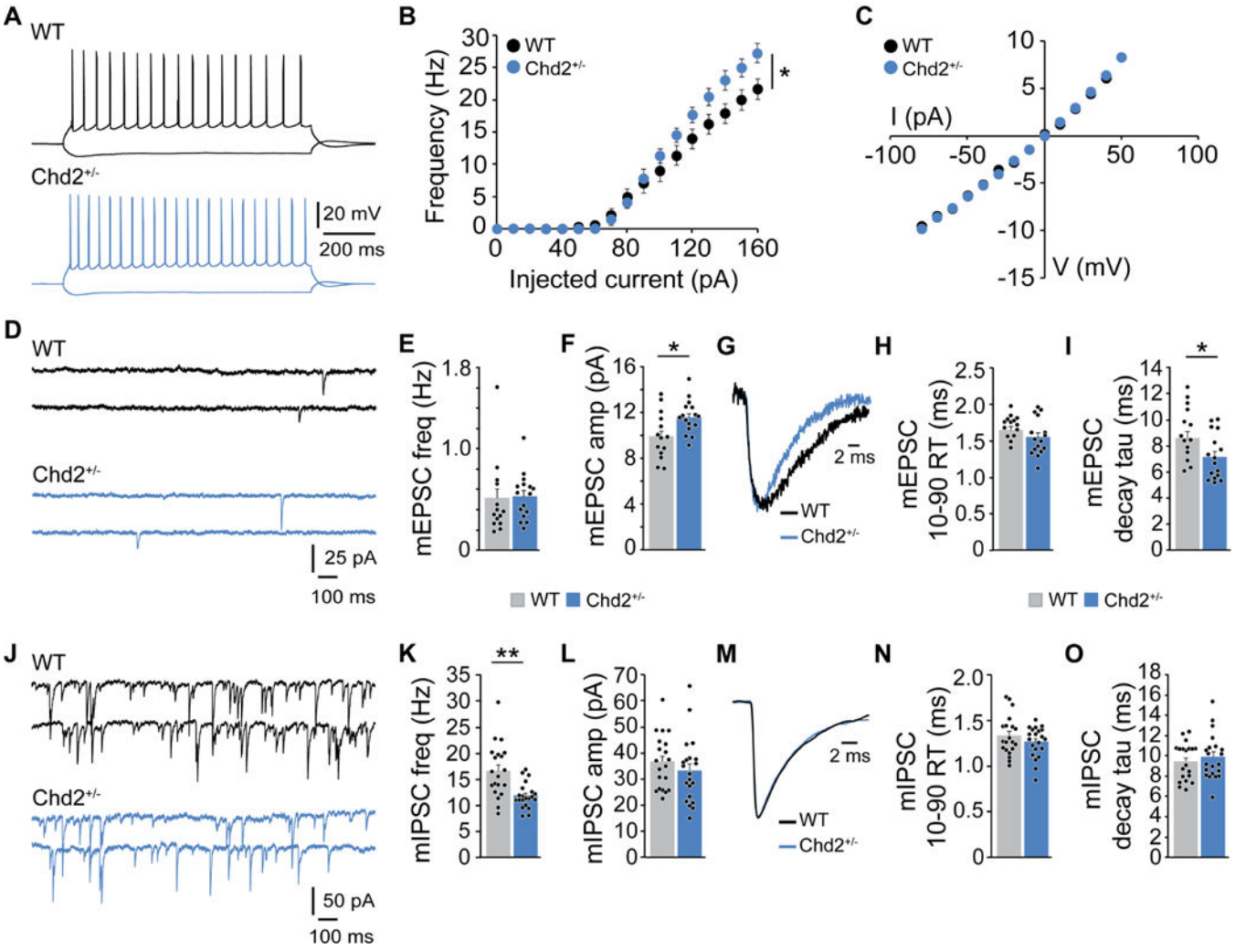

Figure 5. Changes in neuronal excitability and synaptic function in *Chd2*$^{+/-}$ mice.

A. Voltage responses to hyperpolarizing (−80 pA) and depolarizing (+140 pA) current pulses in CA1 pyramidal neurons from a WT (black) and *Chd2*$^{+/-}$ mouse (blue). **B.** Plot of action potential firing frequency (Hz) as a function of current intensity shows increased firing in pyramidal neurons of *Chd2*$^{+/-}$ mice. **C.** Summary current–voltage plot shows R_{input} was not different between groups. Intrinsic electrophysiological properties are summarized in Table S6. **D.** Miniature EPSCs (mEPSCs) recorded from pyramidal neurons in a WT (black) and *Chd2*$^{+/-}$ mouse (blue). **E, F.** At P30–35, mEPSC frequency was unchanged (**E**), but mEPSC amplitudes were increased (**F**) in pyramidal neurons of *Chd2*$^{+/-}$ mice. **G.** Averaged mEPSCs recorded from a pyramidal neuron in a WT (black) and *Chd2*$^{+/-}$ mouse (blue). **H, I.** At P30–35, mEPSC 10–90% rise time (RT) was unchanged (**H**), but mEPSC decay time constant was decreased (**I**) in pyramidal neurons of *Chd2*$^{+/-}$ mice. **J.** Miniature IPSCs (mIPSCs) recorded from pyramidal neurons in a WT (black) and *Chd2*$^{+/-}$ mouse (blue). **K, L.** At P30–35, mIPSC frequency was decreased (**K**), but mIPSC amplitudes were unchanged (**L**) in pyramidal neurons of *Chd2*$^{+/-}$ mice. **M.** Averaged mIPSCs recorded from a pyramidal neuron in a WT (black) and *Chd2*$^{+/-}$ mouse (blue). **N, O.** At P30–35, mIPSC 10–90% rise

time (RT) and decay time constant (tau) were not different between genotypes. Error bars, s.e.m.; ∗ $p < 0.05$; ∗∗ $p < 0.01$. See also Figure S5.

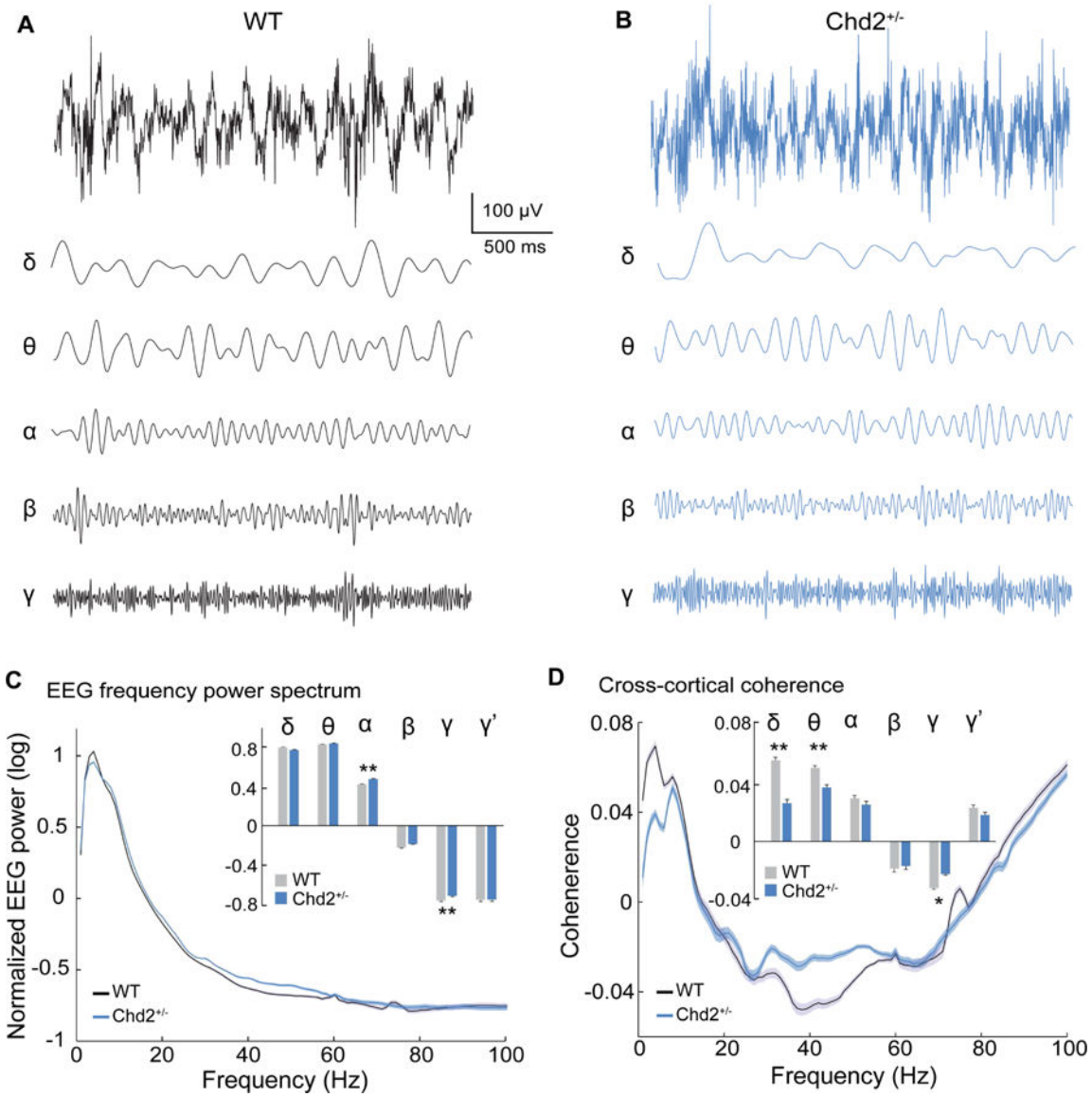

Figure 6. Abnormal rhythmogenesis in *Chd2*$^{+/-}$ mice.

A, B. Example of each frequency band isolated from the local field potential (LFP) in a WT (**A**) and *Chd2*$^{+/-}$ mouse (**B**). **C.** Normalized EEG power spectra. Inset shows mean power for each frequency band (n=5 mice per genotype). **D.** Cross-cortical coherence across the EEG power spectra. Inset shows mean coherence for each frequency band (n=5 mice per genotype). Error bars, s.e.m.; ∗ $p < 0.05$; ∗∗ $p < 0.01$.

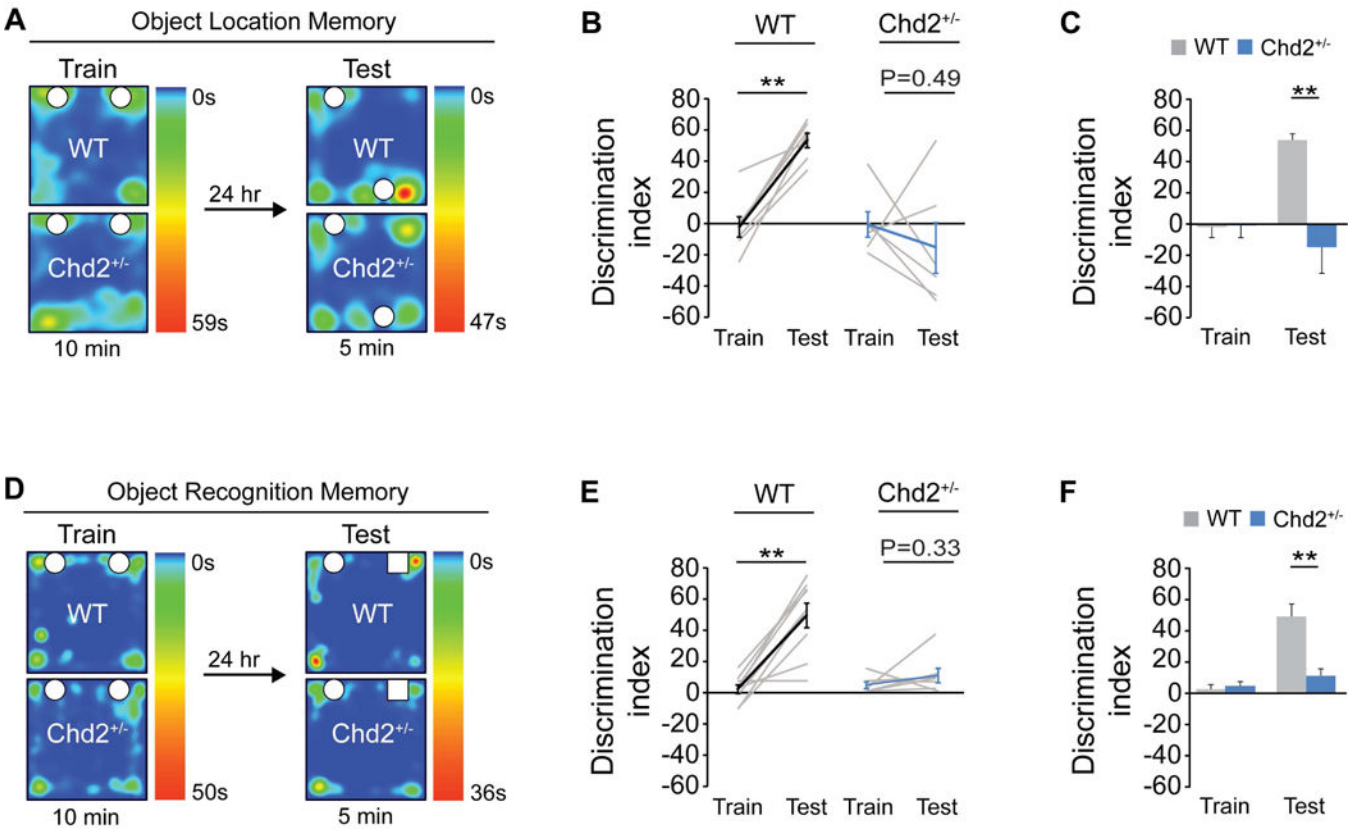

Figure 7. *Chd2*$^{+/-}$ mice exhibit deficits in long-term memory.

A. Heat map showing the location of WT and *Chd2*$^{+/-}$ littermates during the entire training and testing phases of the Object Location Memory (OLM) assay. **B, C.** Discrimination index during training and testing phases of OLM (n=7 WT mice and n=6 *Chd2*$^{+/-}$ mice). **D.** Heat map showing the location of WT and *Chd2*$^{+/-}$ littermates during the entire training and testing phases of the Object Recognition Memory (ORM) assay. **E, F.** Discrimination index during training and testing phases of ORM (n=9 WT mice and n=7 *Chd2*$^{+/}$ mice). Error bars, s.e.m.; ** $p < 0.01$. See also Figure S6 and 7.

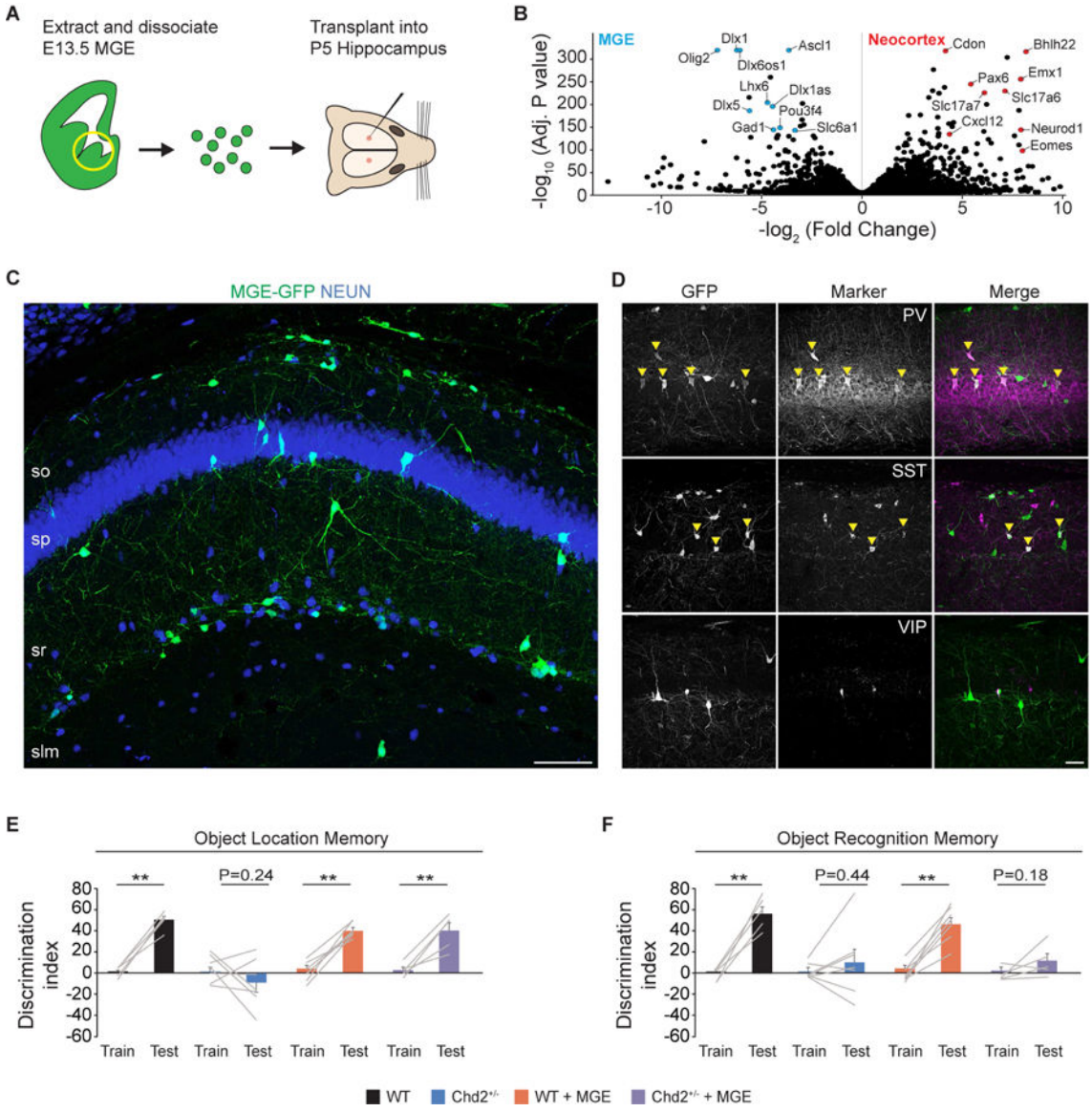

Figure 8. MGE transplantation rescues hippocampal memory problems in *Chd2*$^{+/-}$ mice.

A. Schematic showing the experimental approach used for MGE transplantation. **B.** Volcano plot of differentially expressed genes between E13.5 MGE and neocortex (n = 3 mice per genotype). **C.** Hippocampus of a *Chd2*$^{+/-}$ mouse (45 DAT) labeled for NEUN (blue) and transplanted GFP-labeled inhibitory neurons (green). **D** At 45 DAT, GFP-labeled cells (green) co-expressed PV and SST, but did not express VIP (all in magenta). **E, F.** Discrimination index during training and testing phases of OLM (**E**) and ORM (**F**) assays shows MGE transplantation rescues spatial memory deficits in *Chd2*$^{+/-}$ mice (n=5–7 mice per treatment group). Arrowheads, co-labeled cells; error bars, s.e.m.; ∗∗ $p < 0.01$; scale bars, 100 μm (**C**) and 50 μm (**D**). See also Figure S8.

KEY RESOURCES TABLE

REAGENT or RESOURCE	SOURCE	IDENTIFIER
Antibodies		
β-actin, mouse (1:10000, WB)	Sigma-Aldrich	Cat# A1978, RRID: AB_476692
Chd2, rat (1:300 – 1:500, IF; 1:1000, WB)	Millipore	Cat# MABE873 RRID: AB_2737347
CR, rabbit (1:1000, IF)	Millipore	Cat# AB5054, RRID:AB_2068506
Gad67, mouse (1:200–1:300, IF)	Millipore	Cat# MAB5406, RRID:AB_2278725
GFAP, mouse (1:500, IF)	Millipore	Cat# MAB3402, RRID:AB_94844
GFP, chicken (1:1000, IF)	Aves Labs	Cat# GFP-1020, RRID:AB_10000240
Ki-67, mouse (1:500, IF)	BD Biosciences	Cat# 556003, RRID:AB_396287
NeuN, mouse (1:500, IF)	RD Systems	Cat# MAB377, RRID:AB_2298767
Nkx2.1, rabbit (1:500, IF)	Abcam	Cat# ab76013, RRID:AB_1310784
Olig2, rabbit (1:300, IF)	Millipore	Cat# AB9610, RRID:AB_570666
Pax6, mouse (1:500, IF)	BioLegend	Cat# 901301, RRID:AB_2565003
PV, mouse (1:500, IF)	Sigma-Aldrich	Cat# P3088, RRID:AB_477329
Reelin, mouse (1:500, IF)	Millipore	Cat# MAB5364, RRID:AB_2179313
SST, goat (1:200, IF)	Santa Cruz Biotechnology	Cat# sc-7819, RRID:AB_2302603
Tbr1, rabbit (1:500, IF)	Abcam	Cat# ab31940, RRID:AB_2200219
Tbr2, rabbit (1:500, IF)	Abcam	Cat# ab23345, RRID:AB_778267
Tuj1, mouse (1:1000, IF)	BioLegend	Cat# 801201, RRID:AB_2313773
VIP, rabbit (1:200, IF)	Immunostar	Cat# 20077 RRID: AB_572270
Caspase-3, rabbit (1:500, IF)	Cell Signaling	Cat# 9661S, RRID:AB_2341188
Brn2, mouse (1:500, IF)	Santa Cruz	Cat# sc-393324
Ctip2, rat (1:500, IF)	Abcam	Cat# ab18465 RRID: AB_10015215
Chemicals, Peptides, and Recombinant Proteins		
Bicuculine	Sigma-Aldrich	14343
Kynurenic acid	Sigma-Aldrich	K3375
TTX	Tocris	1078

REAGENT or RESOURCE	SOURCE	IDENTIFIER
Critical Commercial Assays		
Direct-zol RNAMiniPrep Plus kit	Zymo Research	Cat# R2063
NEBNext® Ultra™ RNA Library Prep Kit for Illumina	NEB	Cat# E7530S
Deposited Data		
RNA-sequencing data	This paper	GEO:GSE112196
Experimental Models: Organisms/Strains		
Mouse: Chd2tm1c(EUCOMM)Hmgu	This paper	N/A
Mouse: B6N.FVB-Tmem163Tg(ACTB-cre)2Mrt/CjDswJ	Lewandoski et al., 1997; The Jackson Laboratory	Jax #:003376
Mouse: GAD67-GFP	Tamamaki et al., 2003	N/A
Mouse: C57BL/6J-Tg(Nkx2–1-cre)2Sand/J	Xu et al., 2008	Jax #:008661
Mouse: B6;129S6-Gt(ROSA)26Sortm14(CAG-tdTomato)Hze/J	Madisen et al., 2010	Jax #:007908
Mouse: C57BL/6-Tg(CAG-EGFP)131Osb/LeySopJ	Okabe et al., 1997	Jax#:006567
Mouse: CD-1 IGS Mouse	-	Charles river#:022
Oligonucleotides		
Chd2(tm1c) forward primer: AAGGCGCATAACGATACCAC	Skarnes et al., 2011	N/A
Chd2(tm1c) reverse primer: CCGCCTACTGCGACTATAGAGA	Skarnes et al., 2011	N/A
Chd2(tm1d) forward primer: AAGGCGCATAACGATACCAC	Skarnes et al., 2011	N/A
Chd2(tm1d) reverse primer: ACTGATGGCGAGCTCAGACC	Skarnes et al., 2011	N/A
GFP forward primer: ACGTAAACGGCCACAAGTTC	Tamamaki et al., 2003	N/A
GFP reverse primer: AAGTCGTGCTGCTTCATGTG	Tamamaki et al., 2003	N/A
Cre forward primer: CCGGGCTGCCACGACCAA	Scheel et al., 2003	N/A
Cre reverse primer: GGCGCGGCAACACCATTTTT	Scheel et al., 2003	N/A
Chd2_1 qpcr forward: AGGAGGTCAAATCGAAGCAGA	PrimerBank - MGH-PGA	N/A
Chd2_1 qpcr reverse: GCCTCTTCTTTTCGGACTCCC	PrimerBank - MGH-PGA	N/A
Chd2_2 qpcr forward: CTTCTGAGAGCCAATCAGAGTC	PrimerBank - MGH-PGA	N/A
Chd2_2 qpcr reverse: CATCAGCTATCCGTTCCTTCTT	PrimerBank - MGH-PGA	N/A
Vipr2 qpcr forward: GACCTGCTACTGCTGGTTG	PrimerBank - MGH-PGA	N/A
Vipr2 qpcr reverse: CAGCTCTGCACATTTTGTCTCT	PrimerBank - MGH-PGA	N/A
Hddc3 qpcr forward: CCGCTCACAAACACCGACA	PrimerBank - MGH-PGA	N/A

REAGENT or RESOURCE	SOURCE	IDENTIFIER
Hddc3 qpcr reverse: GCGGCCTGTAACACCACAA	PrimerBank - MGH-PGA	N/A
Myo7a qpcr forward: AGGGGGACTATGTATGGATGGA	PrimerBank - MGH-PGA	N/A
Myo7a qpcr reverse: ATGTGCGTGGCATTCTGAGG	PrimerBank - MGH-PGA	N/A
Slc6a13 qpcr forward: CAGTACACCAACCAGGGAGG	PrimerBank - MGH-PGA	N/A
Slc6a13 qpcr reverse: GCCAGGACAACGATGTAGTAGA	PrimerBank - MGH-PGA	N/A
Ago2 qpcr forward: CGTCCTTCCCACTACCACG	PrimerBank - MGH-PGA	N/A
Ago2 qpcr reverse: CCAGAGGTATGGCTTCCTTCA	PrimerBank - MGH-PGA	N/A
Lgr6 qpcr forward: GAGGACGGCATCATGCTGTC	PrimerBank - MGH-PGA	N/A
Lgr6 qpcr reverse: GCTCCGTGAGGTTGTTCATACT	PrimerBank - MGH-PGA	N/A
Actb qpcr forward: GGCTGTATTCCCCTCCATCG	PrimerBank - MGH-PGA	N/A
Actb qpcr reverse: CCAGTTGGTAACAATGCCATGT	PrimerBank - MGH-PGA	N/A
Software and Algorithms		
pClamp 10.7	Molecular Devices	https://www.moleculardevices.com/systems/conventional-patch-clamp/pclamp-10-software
MiniAnlysis 6.0.7	Synaptosoft	https://www.moleculardevices.com/systems/conventional-patch-clamp/pclamp-10-software
Sigmaplot 13.1	Systat	http://www.synaptosoft.com/MiniAnalysis/
SYSTAT 13.1	SYStat	https://systatsoftware.com/
MATLAB	MathWorks	https://www.mathworks.com/products/matlab.html?s_tid=hp_products_matlab;RRID:SCR_001622
DESeq2	Love et al., 2014	RRID:SCR_015687
ANY-maze	ANY-maze	http://anymaze.co.uk/
Goseq	Young et al., 2010	RRID:SCR_001875
DOSE	Yu et al., 2015	https://bioconductor.org/packages/release/bioc/html/DOSE.html
Goplot	Walter et al., 2015	http://wencke.github.io/
pheatmap	-	https://cran.r-project.org/web/packages/pheatmap/index.html
Other		
4-Channel EEG/EMG Tethered System	Pinnacle Technology	https://www.pinnaclet.com/eeg-emgsystems.html